Supplementary Information

Unravelling the mechanistic complexity of the oxygen evolution reaction and Ir dissolution in highly dimensional amorphous hydrous iridium oxides

Marianne van der Merwe[a], Yonghyuk Lee[b*], Romualdus Enggar Wibowo[a], Tathiana, Kokumai[a], Anna Efimenko[a,c], Mauricio D. Arce[a,d], Catalina E. Jimenez[a], Benjamin Howchen[a], Rosario Suarez Anzorena[a,e], Ilaria Lucentini[f], Carlos Escudero[f], Götz Schuck[g], Zdravko Kochovski[h], Marco Favaro[i], David E. Starr[i], Karsten Reuter[b], Christoph Scheurer[b], Marcus Bär[a,c,j,k], and Raul Garcia-Diez[a*]*

**Corresponding authors*

a. *Interface Design, Helmholtz-Zentrum Berlin für Materialien und Energie GmbH (HZB), Albert-Einstein-Str. 15, 12489 Berlin, Germany.*
b. *Fritz-Haber-Institut der Max-Planck-Gesellschaft, Faradayweg 4 - 6, 14195 Berlin, Germany*
c. *Energy Materials In situ Laboratory Berlin (EMIL), HZB, Albert-Einstein-Str. 15, 12489 Berlin, Germany.*
d. *Departamento Caracterización de Materiales, INN-CNEA-CONICET, Centro Atómico Bariloche, Av. Bustillo 9500, S. C. de Bariloche, Rio Negro, 8400, Argentina*
e. *UNIDEF, CONICET, MINDEF, Departamento de Investigaciones en Sólidos, CITEDEF, J.B. de La Salle 4397, B1603ALO Villa Martelli, Pcia. de Buenos Aires, Argentina*
f. *ALBA Synchrotron Light Source, Carrer de la Llum 2-26, 08290 Cerdanyola del Vallès, Barcelona, Spain*
g. *Department Structure and Dynamics of Energy Materials, HZB, Albert-Einstein-Str. 15, 12489 Berlin, Germany*
h. *Institute of Electrochemical Energy Storage, HZB, Hahn-Meitner-Platz 1, 14109 Berlin Berlin, Germany*
i. *Institute for Solar Fuels, HZB, Hahn-Meitner-Platz 1, 14109 Berlin, Germany*
j. *Department of Chemistry and Pharmacy, Friedrich-Alexander-Universität Erlangen-Nürnberg (FAU), Egerlandstr. 3, 91058 Erlangen, Germany*
k. *Department of X-ray Spectroscopy at Interfaces of Thin Films, Helmholtz Institute Erlangen-Nürnberg for Renewable Energy (HI ERN), Albert-Einstein-Str. 15, 12489 Berlin, Germany*

Table of Contents

The raw data (electrochemical measurements, SEM, cryo-TEM, UHV XPS, *in situ* NAP-HAXPES, and *in situ* and *operando* Ir L_3-edge XAS) and the nanosheet atomic structures utilized in this work have been deposited online in a Zenodo repository that has the following permanent DOI: 10.5281/zenodo.10650051.

Supplementary Note 1. *Charge integration of the cyclic voltammagrams during growth of am-hydr-IrO$_x$*

The controlled growth of highly porous am-hydr-IrO$_x$ was done by the continuous potential cycling of a metallic Ir^0 substrate at 500 mV/s between 0.05 to 1.5 V_{RHE} in 0.5 M H_2SO_4 to a desired number of cycles (**Figure S1**). This results in the monolayer by monolayer electrochemical oxidation of metallic Ir^0 to form a thick iridium oxide layer[6,14]. During HIROF growth, strong evolving redox peaks are observed with increasing growth cycles, which implies a large (evolving) active surface area of the am-hydr-IrO$_x$[4,14].

This phenomenon resulting in the unique shape of the CVs during HIROF growth has been the focus of much research[9,14,26–30] (**Figure S1**) with the current consensus being that the anodic and cathodic peaks correspond to oxidation/reduction processes arising from the newly formed am-hydr-IrO$_x$ and that the peak intensity is linearly correlated with the number of growth cycles.

The unusual observation of the current density in the double-layer region remaining virtually the same during the oxide growth has sparked a lot of debate[9,20,26,31] **Figure S1**). The current hypothesis on this phenomenon is that depending on the applied potential, am-hydr-IrO$_x$ switches between a conductor and a semiconductor, turning "on" at anodic potentials (see *p*DOS in **Figure S18** which shows the Ir 5*d* states extends across the Fermi level for lower H-coverages (i.e., Θ_H = > 0.25 ML) which indicates a conductive nature) and turning "off" (see *p*DOS in **Figure S18** which shows the band gap of the Ir 5*d* states across the Fermi level for the structures with high H-coverages (i.e., Θ_H = 0.50 ML) indicating insulating behaviour) at cathodic potentials. Therefore, the am-hydr-IrO$_x$ layer is active for reactions at anodic potentials (like redox reactions and OER) but is turned "off" for reactions at cathodic potentials (like H_{UPD}). The H_{UPD} therefore only stems from the underlying metallic Ir film. The slight variation in the H_{UPD} region of the metallic Ir substrate and after 1000 cycles of growth to form am-hydr-IrOx is likely related to some surface roughening of the metallic Ir substrate, altering its electrochemically active surface area, that can be expected to occur during the electrochemical cycling growth procedure.

The complementary nature of the double-layer and redox regions of the HIROF's CV has presented a challenge when determining the electrochemical active surface area (ECSA) by the more standard methods. Geiger *et al*.[6] investigated the effect of different integral methods, either including or excluding estimated double layer capacitive charges, on the determined amount and thickness of the oxide layer from the CV. Geiger *et al*.[6] demonstrated that including the entire redox peak area gave results similar to the charge calculated from the concentration of iridium in the electrolyte after formation of HIROF and the subsequent dissolution of the am-hydr-IrO$_x$ layer from the metallic Ir^0 substrate into the electrolyte. Therefore, this work follows the calculation procedures used in several previous works[6,9,32], to estimate the thickness

of the am-hydr-IrO_x layer grown from the thin film Ir^0 electrode, i.e., by assuming that the current increase in the shaded area of **Figure S1** exclusively corresponds to the growth of the am-hydr-IrO_x and that the change in the double-layer capacitance is negligible. **Figure S1** shows the integration area of the cyclic voltammograms obtained at 50 mV/s to determine the charge.

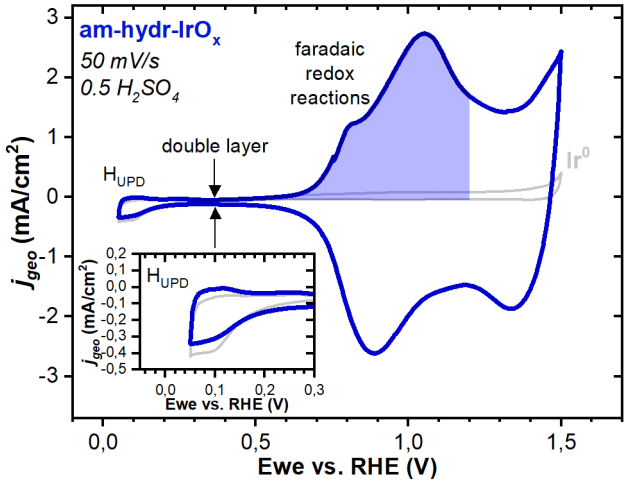

Figure S1. *Charge determination by CV of am-hydr-IrO_x grown ex-situ in a beaker to 1000 cycles. The comparison to the starting metallic Ir substrate is shown in grey, along with the inset to compare the hydrogen underpotential deposition region (H_{UPD}). CV obtained at a scan rate of 50 mV/s in 0.5 M H_2SO_4. The shaded area under the curve indicates the integral area used when estimating the thickness of am-hydr-IrO_x using Faraday's law of electrolysis. The current density is normalized to the geometric area of the electrode.*

Assuming that (1) all Ir atoms undergoing the main redox reaction (shaded area in **Figure S2**) are located in the am-hydr-IrO_x layer (negligible contribution of the theorized native iridium oxide layer present on the metallic Ir^0 substrate), and (2) there is an exclusive occurrence of the $Ir^{3+} \leftrightarrow Ir^{4+}$ transition within the potential region, Faraday's law can be applied to approximate the total charge to a am-hydr-IrO_x layer thickness [6]:

Eq. S1

$$\frac{Q}{n \cdot F} = N$$

where Q is the charge, n is the number of electrons transferred during reaction (n = 1 for the oxidation of Ir^{3+} to Ir^{4+}), F is Faraday's constant, and N is the number of moles electrolyzed, and substituted in for the definition of density and molar mass, where m is mass (g), M_r is the molar mass (g/mol), ρ is density, A is the geometric area of the electrode (cm^2), and d is the thickness of the film (cm), the following version of Faraday's law can be presented as follows:

Eq. S2

$$\frac{Q}{n \cdot F} = N = \frac{m}{M_r} = \frac{\rho \cdot V}{M_r} = \frac{\rho \cdot A \cdot d}{M_r}$$

The charge determined by the integration of the area of the CV is given by the following formula:

Eq. S3

$$\frac{Q}{A} = \frac{1}{v} \cdot \int j \, dV$$

where v is the scan rate of the CV in V/s, j is the current density in A/cm^2. Rearranging **Eq. S2** and substituting into **Eq. S3** gives the following equation for the thickness of the HIROF from the CV:

Eq. S4

$$d_{CV} = \frac{M_r}{\rho \cdot F \cdot v} \int j \, dV$$

A density of 1 g/cm^3 (lower limit as derived from SEM cross-section image determinations) and a molar mass of 224.22 g/mol (M_r of rutile-IrO_2) was assumed for this calculation. A similar calculation was done for the CV obtained of am-hydr-IrO_x after 1000 cycles of HIROF growth in the *in situ* electrochemical cell for the Ir L_3-edge XAS studies (see **Figure S36** for the CV comparison and **Figure S2** for the calculated thickness). It must also be noted that, although it is well established by Cherevko *et al* [8,9] that there is the occurrence of iridium dissolution into the electrolyte within the potential region of HIROF growth, for these calculations, it is assumed that the iridium dissolution amount is negligible compared to the total amount of Ir atoms present in am-hydr-IrO_x undergoing the redox reaction.

The average growth rate is determined as the ratio of thickness to the number of cycles to grow it. This is reasonably stable till ~400 cycles after which it decreases, to a maximum of ~ 30% at 1000 cycles of growth. The non-linear rate of growth (**Figure S3**), determined by the charge transfer integration, also suggests increasing mass and/or charge transport limitations as the am-hydr-IrO_x layer thickness increases [33].

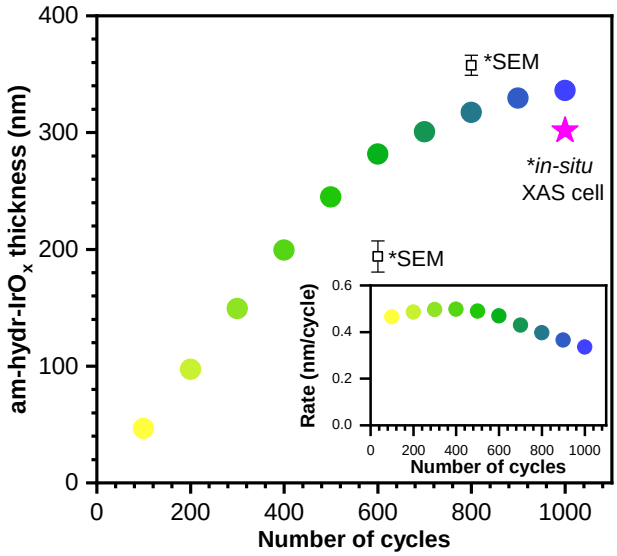

Figure S2. *Am-hydr-IrO_x layer thickness determined using Faraday's law with the charge obtained from integration of the CVs over the $Ir^{3+} \leftrightarrow Ir^{4+}$ redox peak. The inset graph shows the average growth rate, which is defined as the ratio of the thickness with the number of cycles. For comparison, the thickness values derived from cross-section SEM images are also shown The thickness of am-hydr-IrO_x after growth of 1000 cycles in the in situ cell (derived from the charge obtained by integration of the CV shown in* ***Figure S36****) is shown as the magenta star.*

The thickness of am-hydr-IrO_x estimated from the charge integration of the cyclic voltammograms correlates with the thicknesses measured using cross-section Scanning electron microscopy (SEM) images (see **Supplementary Note 2**), validating the choice of density of am-hydr-IrO_x.

Supplementary Note 2. *Thickness and density determination of am-hydr-IrO_x by scanning electron microscopy (SEM) of cross-sections*

Scanning electron microscopy (SEM) of cross-section images show the compact metallic Ir^0 substrate on the Si wafer with the electrochemically grown am-hydr-IrO_x layer on top for **HIROF** grown to 650 and 800 cycles (**Figure S3**). The am-hydr-IrO_x layer displays large micropores consistent with previous findings[1].

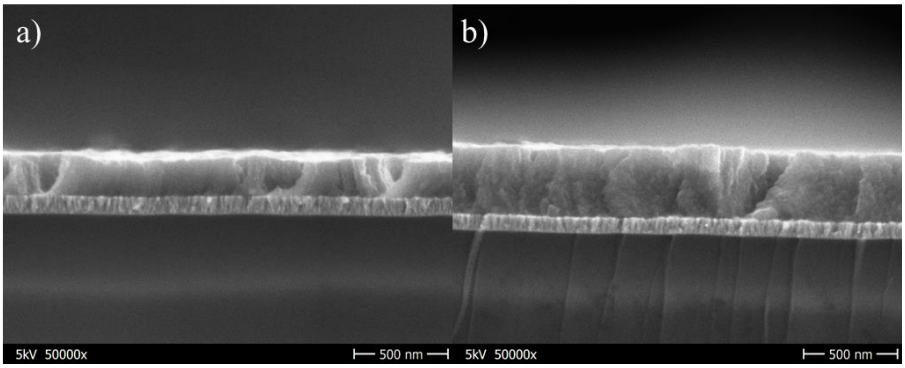

Figure S3. *SEM cross-section images of am-hydr-IrO_x for HIROF grown to (a) 600 and (b) 800 cycles at 500 mV/s in 0.5 M H_2SO_4 from a 100 nm Ir^0 thin film electrode on a Si wafer with a 1.6 µm SiO_2 barrier layer.*

SEM cross-section images were taken to determine the thickness and density of am-hydr-IrO_x. Using ImageJ software[2], the thickness of am-hydr-IrO_x in the samples grown to 600 and 800 cycles were measured to be 194 ± 13 nm and 358 ± 8 nm, respectively. Assuming all of the metallic Ir is oxidized into am-hydr-IrO_x (i.e., there is no or negligible dissolution of iridium into the electrolyte solution), the calculated density of am-hydr-IrO_x is determined by the following formula:

Eq. S5

$$\frac{\rho_{Ir^0} \cdot d_{Ir^0}}{M_{r,Ir^0}} = \frac{n_{Ir^0\ oxidized}}{A_{electrode}} = \frac{n_{am-hydr-IrO_x\ formed}}{A_{electrode}} = \frac{\rho_{IrOx} \cdot d_{am-hydr-IrO_x}}{M_{r,IrOx}}$$

where ρ is the density (g/cm^3), M_r (g/mol) is the molar mass, d is the thickness (cm), $A_{electrode}$ is the area of the electrode (cm^2) and n is the number of moles for metallic Ir (*Ir^0*) and am-hydr-IrO_x, respectively. $n_{Ir^0\ oxidized}$ represents the number of moles of *Ir^0* oxidized into $n_{am-hydr-IrO_x\ formed}$ moles of am-hydr-IrO_x. When **Eq. S5** is rearranged to make the density of am-hydr-IrO_x ($\rho_{am-hydr-IrO_x}$) the subject of the equation, using the measured thicknesses of am-hydr-IrO_x ($d_{am-hydr-IrO_x}$), the change in thickness of the metallic iridium layer (Δd_{Ir^0}), the molar mass of Ir^0 (M_{r,Ir^0}) and am-hydr-IrO_x ($M_{r,IrOx}$, approximated to the molar mass of rutile-IrO_2 = 224.2 g/mol) the following equation is obtained:

Eq. S6

$$\rho_{am-hydr-IrO_x} = \frac{\Delta d_{Ir^0} \cdot M_{r,Ir^0} \cdot \rho_{Ir^0}}{d_{am-hydr-IrO_x} \cdot M_{r,am-hydr-IrO_x}}$$

The calculated density of ~1 – 2 g/cm^3, which corresponds well to previous optical and coulometric measurements[1,3,4] estimations of 1 – 2 g/cm^3. This means that for every 1 nm of metallic iridium that is electrochemically oxidized, an average of 26.4 nm of am-hydr-IrO_x is grown.

Supplementary Note 3. *Activity comparison of am-hydr-IrO_x with Ir^0 and IrO_2 references*

Comparison of the electrochemical behaviour of am-hydr-IrO_x, metallic Ir^0 and rutile-IrO_2 is shown in **Figure S4a**. The OER activity of am-hydr-IrO_x is compared to the activity of thin film metallic Ir^0 and rutile-IrO_2 electrodes, by means of linear sweep voltammetry at 10 mV/s from 1.30 to 1.60 V_{RHE} (see **Figure S4b**). Am-hydr-IrO_x displays much higher current density compared to rutile-IrO_2. The higher activity of am-hydr-IrO_x compared to rutile-IrO_2 is a result of: **(i)** different Ir and O species composition of am-hydr-IrO_x and rutile-IrO_2 (implying different theorized active sites) and **(ii)** a much higher electrochemically active surface area of am-hydr-IrO_x compared to rutile-IrO_2. The entire volume of the am-hydr-IrO_x layer is considered to be active whereas mainly the surface of rutile-IrO_2 is active, although there are reports of pit-corrosion showing activity in the first 2.5 nm of the compact IrO_2 layer[5].

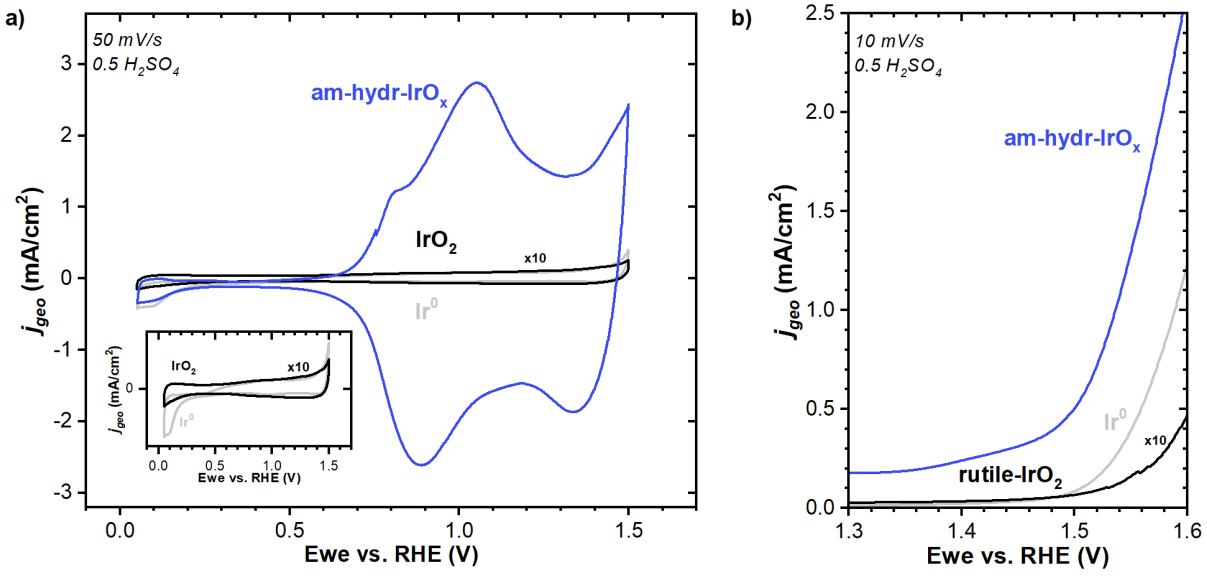

Figure S4*. a) Cyclic Voltammetry obtained with a scan speed of 50 mV/s and b) Linear sweep voltammetry obtained with a scan speed of 10 mV/s of Ir^0 in grey, rutile-IrO_2 in black (magnified by a factor of ×10) and am-hydr-IrO_x (growth to 800 cycles) in blue. Am-hydr-IrO_x demonstrates a higher OER activity compared to Ir^0 and rutile-IrO_2 with the highest current density at E = 1.60 V_{RHE}. The current density is normalized to the geometric area of the electrode.*

The electrochemical behaviour of am-hydr-IrO_x in comparison with metallic Ir and rutile-IrO_2 is presented normalized to the geometric area thus enabling direct comparisons to the extensive number of studies already done on the activity and stability of am-hydr-IrO_x[5–9].

The higher current density within the region of ~1.3 – 1.45 V_{RHE} compared to the metallic Ir^0 substrate from which am-hydr-IrO_x is grown is related to the redox charge transfer reactions as also previously observed[9].

Supplementary Note 4. *In situ 'dip-and-pull' NAP-HAXPES of am-hydr-IrO_x*

S4.1. Electrode preparation for 'dip-and-pull' NAP-HAXPES

For the performance of a 3-electrode 'dip-and-pull' experimental configuration for NAP-HAXPES measurements, a metallic iridium electrode with a rough surface is preferable, since it possesses enhanced wettability compared to a smooth Ir electrode prepared by sputter deposition. The increased electrode roughness facilitates the formation of the thin electrolyte film on top of the metallic Ir electrode following the "dip-and-pull" process, which is necessary for *in situ* NAP-HAXPES measurement at the electrode|thin electrolyte layer interface. This rough iridium electrode was prepared via electrodeposition of metallic iridium on a clean Au foil. The electrodeposition procedure used in this work is based on the protocol described in Sawy *et al.* (2009) and (2013) to deposit a uniform, highly porous metallic iridium layer onto a Au substrate [10,11].

A 0.25 mm thick Au foil (99.95% Alfa Aesar), 0.5 cm wide and 5 cm long was used as substrate for the Ir electrodeposition. The Au foil was first cleaned by potential cycling between 0.05 and 1.6 V_{RHE} at 50 mV/s in 0.5 M H_2SO_4 for 50 cycles. A Ag|AgCl|$KCl_{(sat.)}$ reference electrode and a 1×1 cm Pt mesh (52 mesh woven, 0.1 mm diameter wire, 99.9% Alfa Aesar) as the counter electrode were used. A solution of 1 mM H_2IrCl_6 in 0.5 M H_2SO_4 was then prepared by adding H_2IrCl_6 (99.95%, Sigma Alrich) to the 0.5 M H_2SO_4 solution. Each solution was deaerated by N_2 bubbling for 30 min prior to each experiment. Electrodeposition of metallic Ir onto the lower 4 cm part of the Au electrode was carried out at a potentiostatic voltage of 0.18 V_{RHE} for 3 hours. This left 1 cm of uncoated Au at the top of the electrode, which was used for energy calibration of the NAP-HAXPES measurements. After electrodeposition, the electrode was removed from the solution, rinsed thoroughly with de-ionized water, and the CV response of the electrode was obtained between 0.05 and 1.5 V_{RHE} in a fresh 0.5 M H_2SO_4 solution. **Figure S5** shows the CV responses of the Au electrode after cleaning (**a**), and after the electrodeposition of the metallic iridium (**b**). Using Faraday's law and the average current drawn during the potential hold at 0.18 V_{RHE}, the thickness of the electrodeposited Ir^0 is estimated as 6.9 µm, assuming the density of a compact layer of metallic iridium of 22.56 g/cm^3.

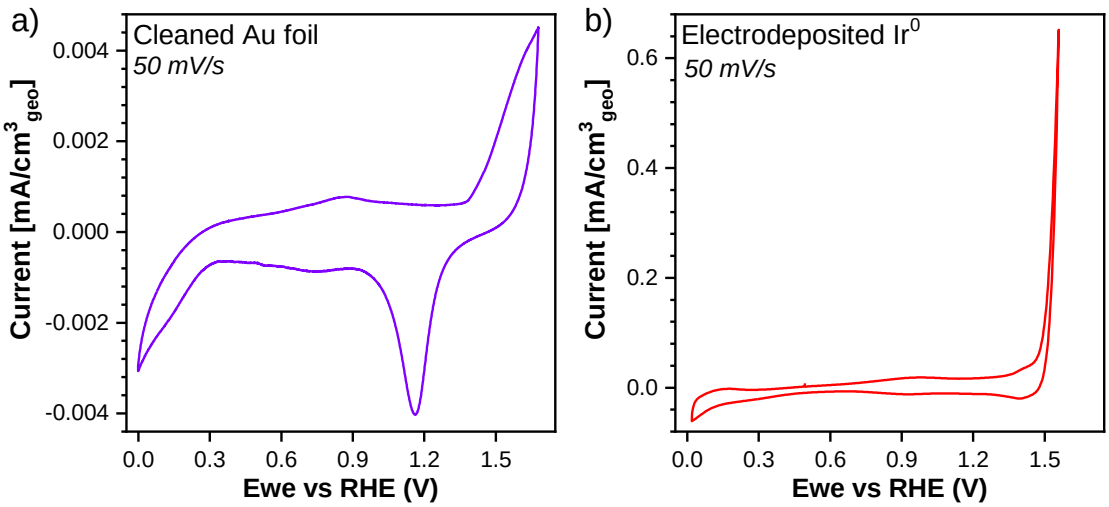

Figure S5. *CVs of cleaned Au foil and electrodeposited Ir^0 performed with the scan rate of 50 mV/s in 0.5 M H_2SO_4.*

S4.2. Experimental configuration of the SpAnTeX endstation

The 3-electrode 'dip-and-pull' experimental configuration of the SpAnTeX end-station [12] is shown in **Figure S6**. The iridium electrode is connected to the sample manipulator such that a large portion of Au is still visible (i.e., not immersed in the electrolyte). This provides a reference for energy calibration of the NAP-HAXPES data. Prior to NAP-HAXPES measurements, the iridium electrode was first measured in vacuum to characterize the initial electronic configuration. Thereafter, the 0.5 M H_2SO_4 solution was introduced, and the chamber was pumped down and kept at a steady pressure of 12 mbar. The electrodes are dipped into the 0.5 M H_2SO_4 solution and retracted to form a thin film of electrolyte on the surface.

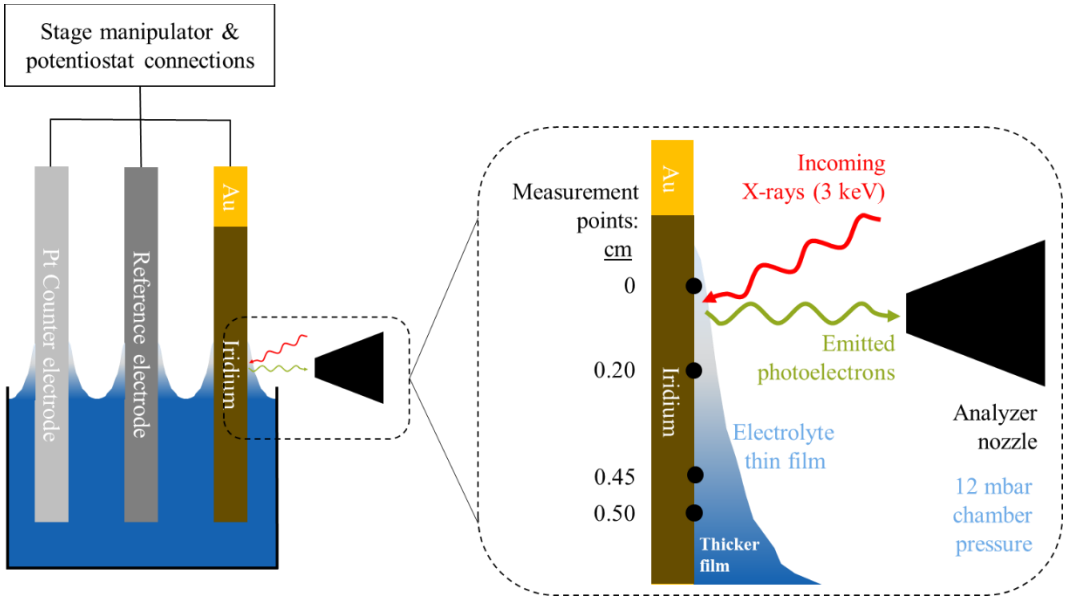

Figure S6. *NAP-HAXPES 'dip-and-pull' experimental configuration with 3-electrode setup. Measurements were taken along the length of the iridium electrode after 'dip-and-pull'. Measurement positions are shown relative to the topmost measurement position (i.e., position "0") of the electrolyte thin film, where only a metallic Ir signal (i.e., Ir^0) was observed).*

S4.3. *In situ* electrochemical growth of am-hydr-IrO_x

The electrode is initially fully dipped into the beaker, after which 3 cycles of HIROF growth were performed to initiate the formation of am-hydr-IrO_x. The electrode was then retracted to form the thin film of electrolyte, and the growth was continued till 44 cycles in total. The electrode was then subjected to further HIROF growth potential cycling between 0.05 – 1.5 V_{RHE} at 500 mV/s to form more am-hydr-IrO_x from the electrodeposited iridium electrode. **Figure S7** depicts the growth CVs. The growth was stopped after 44 cycles, since due to the hydrophilic nature of the am-hydr-IrO_x layer, the electrolyte layer becomes too thick to probe through and observe the metallic Ir species. Based on the calibration curve from **Figure 1d**, the thickness of the grown am-hydr-IrO_x layer can be estimated from the number of HIROF growth cycles performed to be roughly 21 nm. Thickness of am-hydr-IrO_x is approximated with this method, since in this experiment the surface area cannot be accurately determined, and thus the estimation of the amount of am-hydr-IrO_x formed using the charge (by integration of the CV) is not possible. The arrows indicate the increase in the signal of the redox couple for the anodic and cathodic sweeps, and the decrease in the hydrogen under potential deposition region like **Fig. 1 a)**. This is characteristic of HIROF growth[6,13,14].

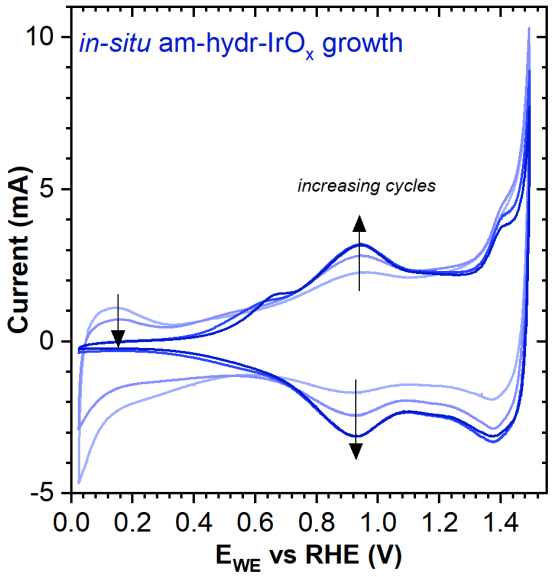

Figure S7. *CVs during the in situ growth of am-hydr-IrO_x from a electrodeposited iridium electrode in a 3-electrode 'dip-and-pull' configuration for NAP-HAXPES measurements. The CVs were performed with a scan rate of 500 mV/s. The current is shown in mA as determination of the wetted geometric area of the electrode (both thin film and bulk immersed portions) is not possible.*

S4.4. *In situ* NAP-HAXPES Ir 4f and O 1s measurements

NAP-HAXPES measurements were made along the length of the dipped electrode at regular intervals, see **Figure S6**. The zero position was determined at the top of the electrode where a metallic iridium species identified by Ir 4f measurements was visible, and the O 1s signal showed –OH and H_2O intensities that indicated the presence of a very thin film of electrolyte. The measured positions extend with depth into the increasing electrolyte thin film. The lower limit of the measurement point was determined by the disappearance of the Ir 4f spectrum due to attenuation by a (too) thick electrolyte layer.

The Ir 4f and O 1s core level spectra are shown in **Figure S8.** Next to the Ir 4f spectra are schematics (not to scale) of the layer configurations and probing depths of the measurements. With positions down the length of the electrode (i.e., with increasing electrolyte thin film thickness), the Ir 4f peak shifts from a binding energy characteristic of metallic iridium (60.9 eV) to a binding energy of 62.5 eV, which is similar to that of the predicted trivalent Ir-defect site in rutile-IrO_2 [15–17]. There is a very low intensity at a binding energy of 61.8 eV associated with Ir^{4+} species. The O 1s spectra show that there is no difference in intensities of the lattice O, -OH, and H_2O contributions within positions down the length of the electrode. Unfortunately, deconvolution of the contribution of –OH and H_2O signals coming from the thin film electrolyte layer and –OH and H_2O signals coming from the porous am-hydr-IrO_x layer, is very challenging due to several reasons: **(1)** the OH species in the spectra can arise from Ir-OH bonds in the material or due to the interaction of water with the surface of the material, **(2)** the am-hydr-IrO_x layer is very porous, so the H_2O signal arises from water in the two layers, the thin film electrolyte layer and the water inside the porous am-hydr-IrO_x layer, and **(3)** there is also the contribution of chemisorbed H_2O for which its contribution is dependent on the surface area of the material, which is large in the case of am-hydr-IrO_x. For these reasons, the electrolyte layer thickness also cannot be estimated from the NAP-HAXPES measurements. From **Figure S8b**, it can only be said that the film itself is highly hydrated, and a very low contribution of lattice O bonds are observed, which is in accordance with the UHV Al K_α XPS measurements, see **Figure 1a**.

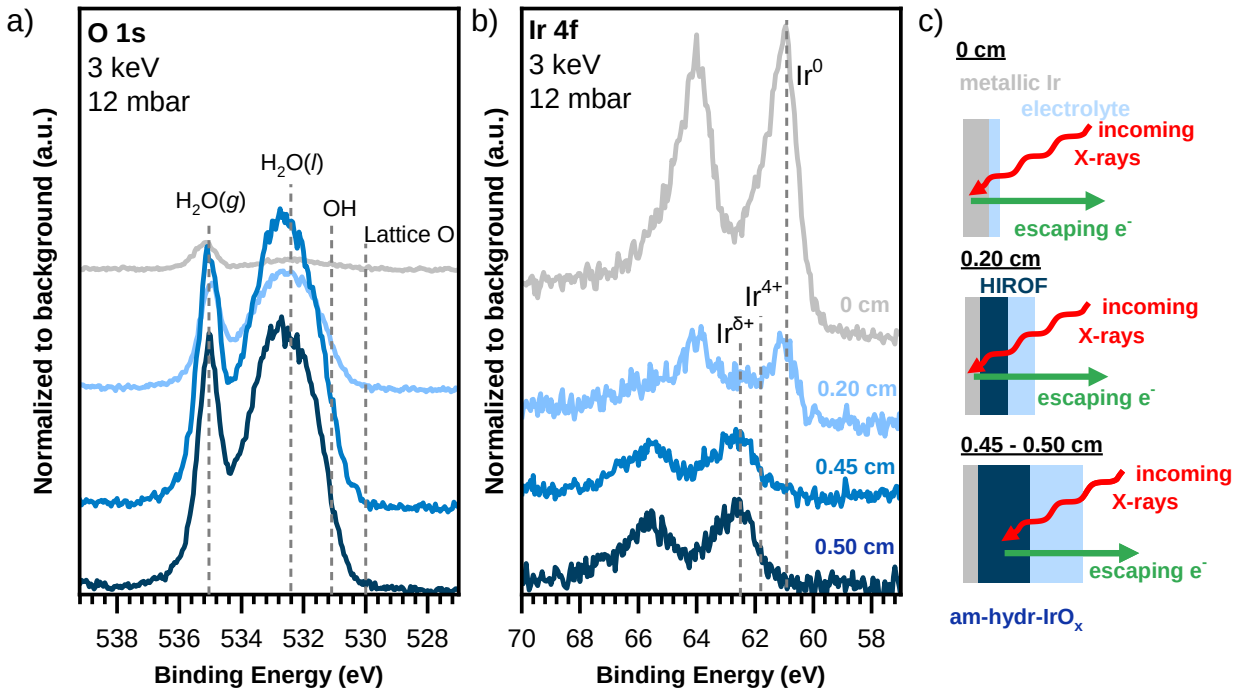

Figure S8. *In situ NAP-HAXPES measurements using a photon energy of 3 keV, at 12 mbar of the a) O 1s and b) Ir 4f core level at different positions along the electrode. (c) Schematics depicting how the limited probing depth affects to ability to probe the different layers (metallic iridium, am-hydr-IrO_x, and electrolyte) as a function of measurement spots going down the "dip-and-pulled" electrode. See* ***Figure S6*** *for a schematic of the "dip-and-pull" setup. Four O 1s spectral components are indicated by vertical dashed lines in a) namely, lattice O, -OH, $H_2O(l)$ and $H_2O(g)$. Three Ir 4f spectral components are indicated by vertical dashed lines in a) namely, Ir^0 (metallic Ir), Ir^{4+} (rutile-IrO_2), and $Ir^{\delta+}$ (am-hydr-IrO_x).*

The NAP-HAXPES Ir 4f spectra were fitted with three finite Lorentzian profiles to represent the three identified Ir species (Ir^0, Ir^{4+}, and $Ir^{\delta+}$ representing am-hydr-IrO_x). The Ir 4f doublet peak areas were constrained to a ratio of 4:3 and doublet peak separation of 3.0 eV was used for the fit[18,19]. The LF line shape parameters were kept the same for both the $4f_{7/2}$ and $4f_{5/2}$. The line shape parameters of the Ir^0 species is determined by the fit of the Ir 4f spectra at the topmost position (i.e., "0 cm") alone, i.e., the position that is dominated by the structure of the metallic iridium electrode. Since there is no reference measurement of IrO_2 available under similar conditions, it was assumed that the Ir^{4+} and $Ir^{\delta+}$ species would have similar LF line shape parameters and were therefore constrained to be the same. The fits and line shape parameters for the Ir^{4+} and $Ir^{\delta+}$ species were determined by performing a simultaneous fit of the entire data (i.e., minimizing the residuals of the entire dataset). The fitted line shape parameters are shown in **Table S1**. By correcting the fitted peak areas for the atomic density of each of the species (determined by the molar mass and density of the material), the relative contribution of Ir^{4+} is calculated to be lower than 0.9%.

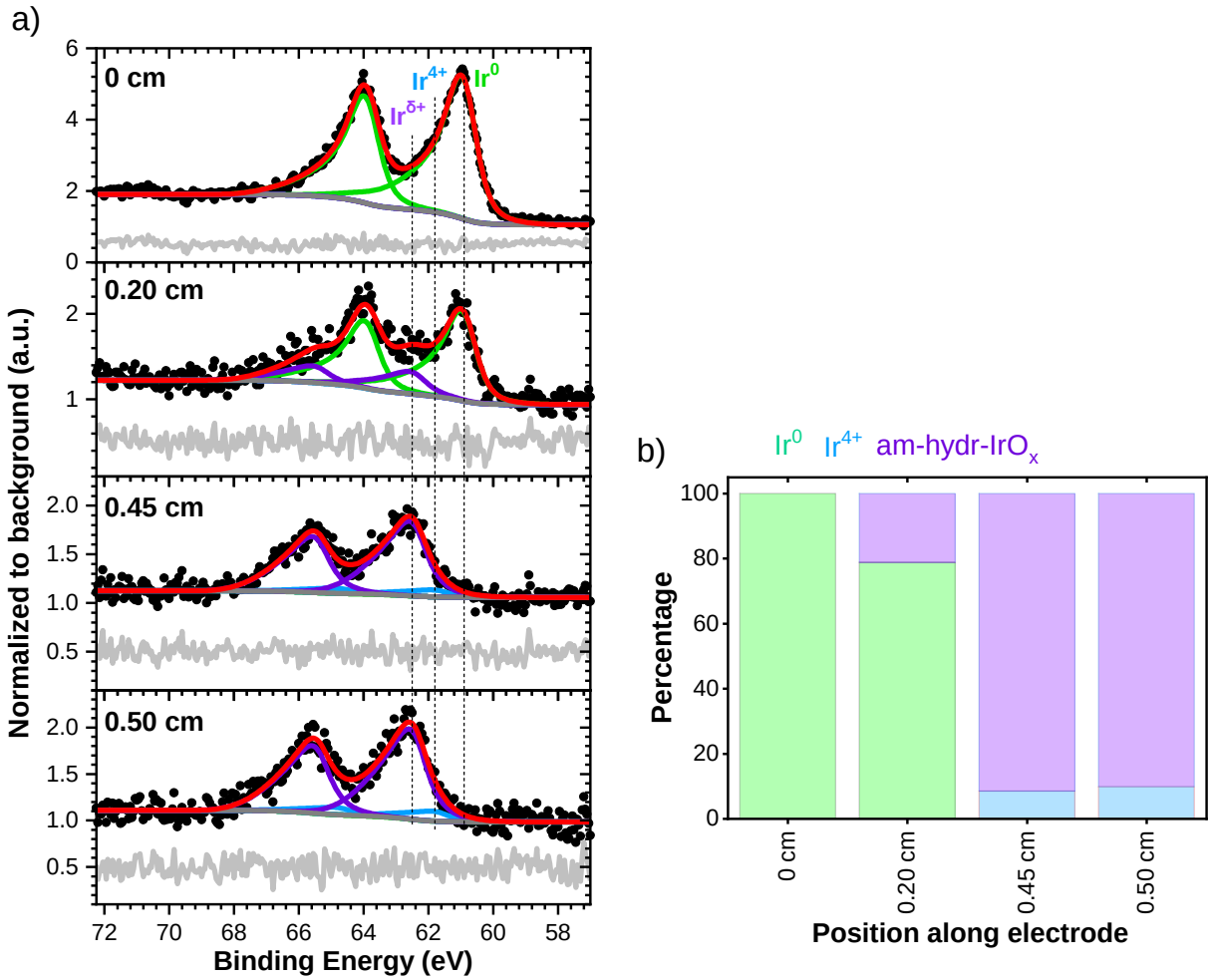

Figure S9. *In situ NAP-HAXPES measurements using a photon energy of 3 keV, at 12 mbar. a) fit of the Ir 4f core level measured along different positions along the electrode using three Ir species (Ir^0, Ir^{4+} and $Ir^{\delta+}$ representing am-hydr-IrO_x) with a finite Lorentzian lineshape profiles, and b) the relative composition of the three identified species.*

Table S1 tabulates the Ir $4f_{7/2}$ BEs and LF line shape parameters employed for the model to fit Ir^0, IrO_2 and am-hydr-IrO_x based on approaches used in Ref.[19] and **Figure S7** presents the fitted Ir 4f spectra.

Table S1 *Finite Lorentzian line shape profile parameters were used to fit the NAP-HAXPES Ir 4f peaks by three components ascribed to the Ir^0, Ir^{4+} representing IrO_2, and $Ir^{\delta+}$ representing am-hydr-IrO_x.*

	Ir^0	**Ir^{4+}**	**$Ir^{\delta+}$**
Ir $4f_{7/2}$ center (eV)	60.9	61.8	62.5
α	0.40	0.27	0.27
γ	0.55	0.90	0.90
β	1	1	1
m	1.3	0.95	0.95
w	842	217	217
FWHM (eV)	1.25	1.60	1.60

Note, that the contribution of Ir $5p_{1/2}$ peak, which lies underneath the Ir 4f peak, was excluded due to low peak intensity of the Ir $5p_{3/2}$ peak.

The surface morphology of the electrodeposited Ir^0 and grown am-hydr-IrO_x layer was investigated using SEM. **Figure S10a** shows the top-view SEM images of the surface of the electrodeposited Ir^0. The electrodeposition of the Ir^0 results in the formation of high surface roughness with the formation of spherical islands. **Figure S10** shows the difference in the surface morphology after the formation of am-hydr-IrO_x by HIROF growth (**b**) the electrolyte thin film portion of the electrode and (**c**) the portion of the electrode that was immersed in the bulk of the electrolyte solution. The difference in surface morphology indicates a difference in the growth rate in the electrolyte thin film and bulk solution submerged parts of the electrode, likely due to different mass transport properties at bulk solution and thin film region, as reported in some previous works.

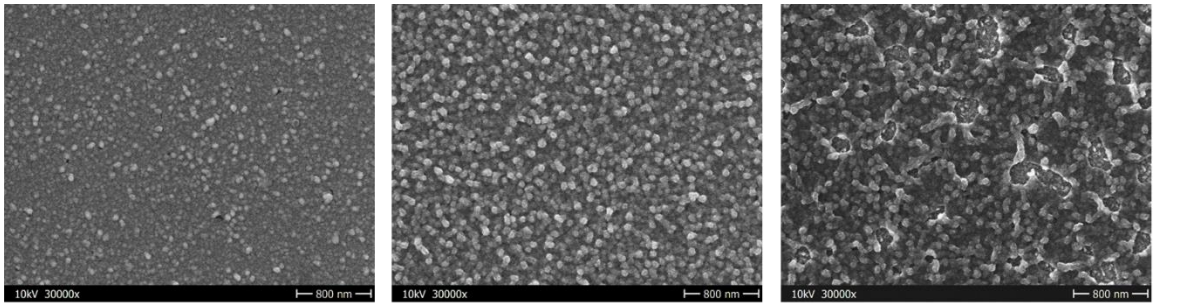

Figure S10. *Top view SEM images of the a) electrodeposited Ir^0, and formation of am-hydr-IrO_x by growth of HIROF in b) the thin film electrolyte portion and c) the bulk solution portion of the electrode in the 'dip-and-pull' configuration for the NAP-HAXPES measurements.*

Supplementary Note 5. *UHV Al K_α XPS*

S5.1. Sample preparation and XPS measurement details

Ultra-high vacuum (UHV) Al K_α excitation x-ray photoelectron spectroscopy (UHV Al K_α XPS) was performed to investigate the electronic structure of am-hydr-IrO_x. O 1s and Ir 4f core level spectra were measured with a pass energy of 20 eV while a pass energy of 100 eV was used for survey spectra.

Multiple am-hydr-IrO_x samples were grown to different number of cycles *ex-situ*, the samples were then rinsed with DI water and dried in the Ar-filled glovebox antechamber (10^{-3} mbar) for ~2 hours prior to XPS measurements. Binding energy calibration was performed using a clean Au foil, setting the Au $4f_{7/2}$ peak to 84.00 eV or using a clean Ir^0 thin film, setting the Ir $4f_{7/2}$ peak to 60.9 eV[18]. Reference measurements were conducted on Ir^0 and rutile-IrO_2 thin films.

S5.1. O 1s spectra

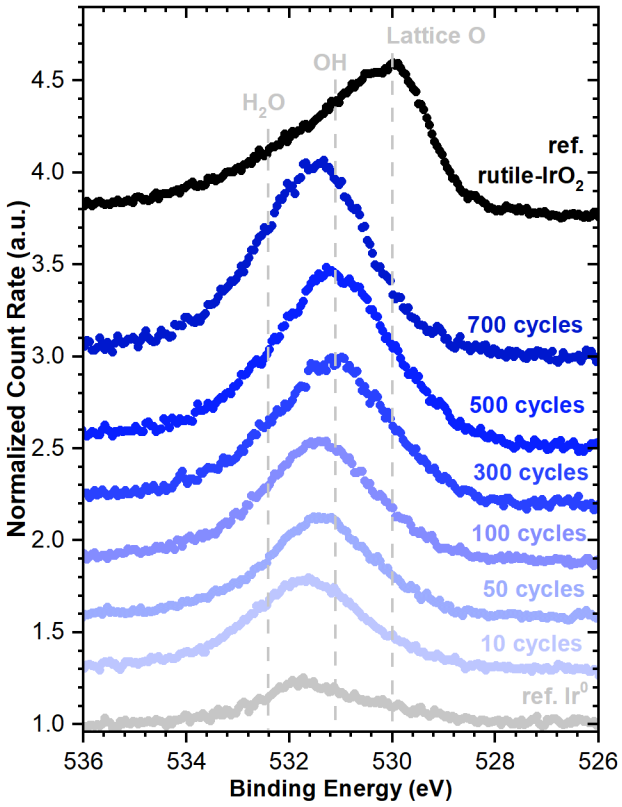

***Figure S11**. O 1s spectra of am-hydr-IrO_x from HIROF samples grown to different cycle numbers (10, 50, 100, 300, 500, & 700 cycles). Reference spectra for Ir^0 and rutile-IrO_2 are shown for comparison.*

The O 1s spectra am-hydr-IrO_x measured under UHV conditions indicate that several species exist, namely lattice-O, hydroxyl group (-OH) and chemisorbed H_2O. The reference lines for lattice-O, -OH, and H_2O are taken from Ref.[15,19,20]. Oxygen is present predominantly in the form of hydroxyl bonding in am-hydr-IrO_x although there is appreciable lattice-O spectral intensity. This is likely related to the UHV induce dehydration of the am-hydr-IrO_x.

S5.1. Ir 4f spectra

Am-hydr-IrO_x presents broader asymmetric Ir 4*f* peaks, which signifies an (oxy)-hydroxide nature with mixed iridium states, distinct from the rutile-IrO_2 standard which has narrower asymmetric peaks (Ir $4f_{7/2}$ = 61.4 eV) indicating a single Ir^{4+} species (**Figure S12**).

The Ir 4*f* spectra were fitted using the LMFIT Python package[21] using asymmetric Finite Lorentzian (LF) lineshapes[22]. Note, that contributions of Ir $5p_{1/2}$ peak, which lies underneath the Ir 4*f* peak, were excluded due to the low photoionization cross-section ratios[23].

The Ir 4*f* spectra of the reference Ir^0 and rutile-IrO_2 thin films were first fitted to determine their LF parameters, which are consequently used in fittings of the am-hydr-IrO_x spectra. The Ir 4*f* doublet peak areas were constrained to a ratio of 4:3 with a doublet separation of 3.0 eV[18,19], and the same line shape for both the $4f_{7/2}$ and $4f_{5/2}$ peaks. After the line shape parameters and binding energies for the Ir^0 and Ir^{4+} species were determined, the am-hydr-IrO_x spectra (grown to 10, 50, 100, 300, 500 & 700 cycles) was fitted using three pairs of finite Lorentzian line shapes to model the three different iridium species present: Ir^0, Ir^{4+} and $Ir^{\delta+}$ representing am-hydr-IrO_x. The line shape parameters for the Ir^0 and Ir^{4+} species pairs were constrained to previously determined values from reference Ir^0 and IrO_2 thin films, while those for am-hydr-IrO_x were allowed to vary. The fits and line shape parameters for am-hydr-IrO_x were determined by performing a simultaneous fit of the entire data (i.e., minimizing the residuals of the entire dataset).

Table S2 tabulates the Ir $4f_{7/2}$ BEs and LF line shape parameters employed for the model to fit Ir^0, IrO_2 and am-hydr-IrO_x based on approaches used in Ref.[19] and **Figure S12** presents the fitted Ir 4f spectra.

Table S2 *Finite Lorentzian lineshape parameters and Ir $4f_{7/2}$ binding energies of Ir^0, IrO_2, and $Ir^{\delta+}$ representing am-hydr-IrO_x.*

	Ir^0	**Ir^{4+}**	**$Ir^{\delta+}$**
Ir $4f_{7/2}$ center (eV)	60.8	61.3	62.1
γ	1.12	0.87	1.17
α	0.76	0.31	0.40
β	1.367	1.00	1.00
m	1.00	1.40	1.61
w	1000	1000	1000
FWHM (eV)	1.30	1.55	1.80

Rutile-IrO_2 possesses a narrow Ir 4*f* peak width (LF parameters γ = 0.87, m = 1.40) and a more asymmetric line shape (LF parameter ratio of α = 0.31, β = 1.00) compared to am-hydr-IrO_x which possesses a broader Ir 4*f* peak width (LF parameters γ = 1.17, m = 1.61) and a less asymmetric line shape (LF parameter ratio of α = 0.40, β = 1.00); this correlates well with what is observed in other studies[15,19,24]. The broadening related to the Ir sub-oxide species appearance is given by the larger Full Width Half Maximum (FWHM) in the last row of the table. Both the shift in the Ir 4*f* and the peak shape indicate different electronic environments.

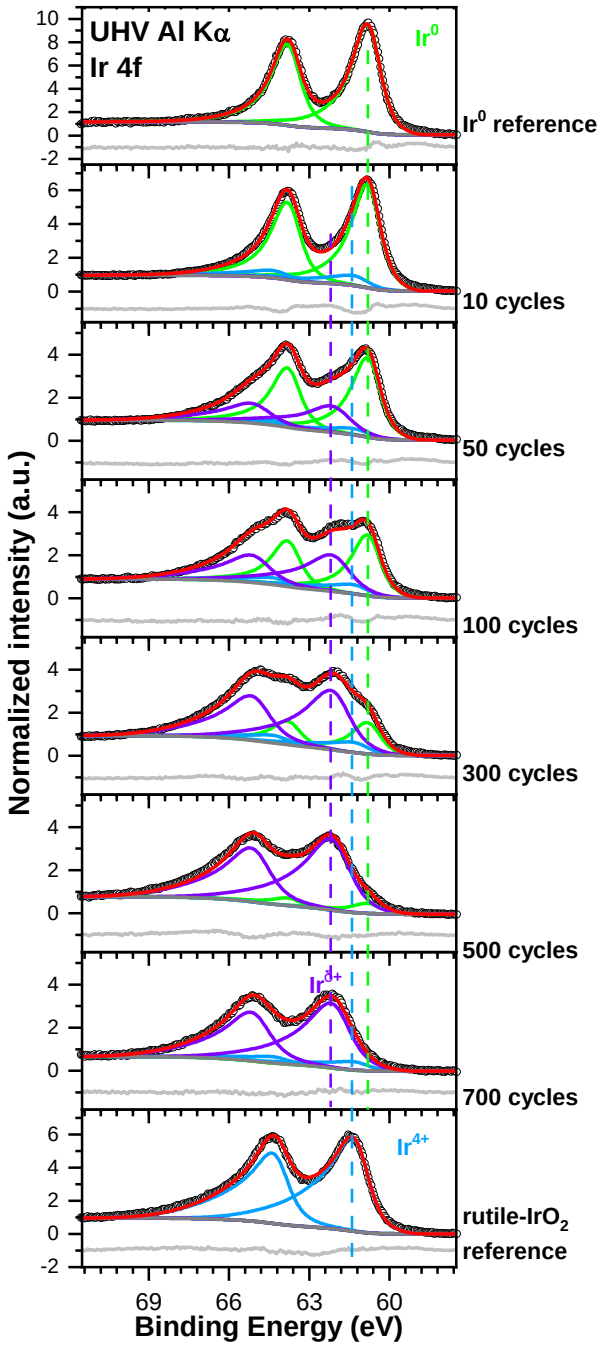

Figure S12. *Fits of the UHV Al K⍺ XPS Ir 4f data of am-hydr-IrO_x grown to different cycle numbers (10, 50, 100, 300, 500, & 700 cycles). Reference spectra for Ir^0 and rutile-IrO_2 thin films are shown for comparison. Three spectral components ascribed to Ir^0 (metallic Ir) in green, Ir^{4+} (rutile-IrO_2) in blue, and $Ir^{\delta+}$ (am-hydr-IrO_x) in purple were fitted.*

From the fits shown in **Figure S12**, the percentage contributions of each of the iridium species can be determined by their peak areas. **Figure S13** below summarizes the contributions of the different iridium species in HIROF grown to different number of cycles (10 to 700 cycles), measured in UHV conditions. The compositions of the metallic iridium and rutile-IrO_2 thin film reference are depicted for comparison.

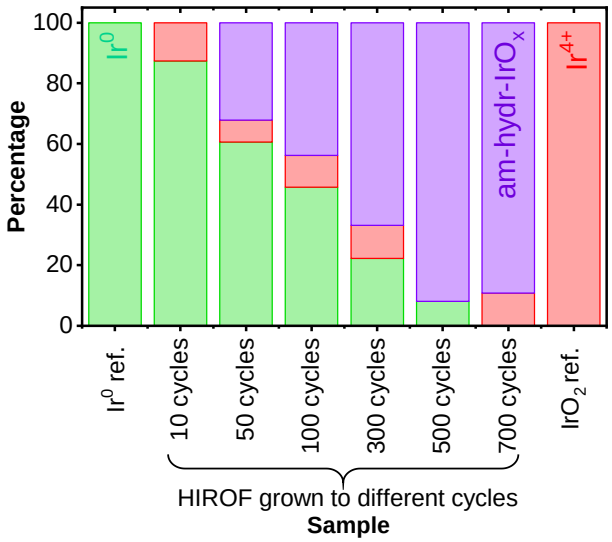

***Figure S13**. Relative composition of the iridium species identified from of HIROF layers grown to different number of cycles ($HIROF_{10}$ to $HIROF_{700}$). The derived composition of Ir^0 and IrO_2 reference samples is shown for comparison.*

The contribution of the Ir^{4+} species in am-hydr-IrO_x is presumably formed due to the vacuum drying conditions inducing dehydration of the film[6].

Supplementary Note 6. *EXAFS fits of the Ir L_3-edge EXAFS spectra obtained during preparation of am-hydr-IrO_x by HIROF growth*

S6.1. EXAFS fitting procedure

Fitting of the *in situ* Ir L_3-edge EXAFS data collected during HIROF growth to 1000 cycles was performed using a two-component structural model consisting of *fcc*-elemental Ir to model the metallic Ir substrate, along with rutile-IrO_2 structure as an initial approximation for the am-hydr-IrO_x component in HIROF (this structural was later replaced by the nanosheet model and compared, see **section S5.2.**). A linear combination of the first shell scattering paths was employed to determine the relative weight of the metallic Ir scattering path, which can be approximated with the nominal concentration of the metallic Ir within the sample environment.

Larch software[25] was used to perform the EXAFS fits over k = 3 – 11 $Å^{-1}$ and R = 1 – 3.5 Å, which covers the range of the scattering peaks of the first coordination shells. Only the scattering paths for the first coordination shells of the *fcc*-Ir^0 and rutile-IrO_2 structures were used (see **Table S6**). The energy shift (ΔE_0) and the Debye-Waller (σ) parameters were kept unrestricted, while the interatomic distances (R), and coordination numbers (*CN*) were kept fixed. This results in a rigid fitting approach. The passive electron reduction factors (S_0^2) of the two structures were calculated as follows:

Eq. S7

$$S^2_{0,metallic\ Ir} = amp_{metallic\ Ir} \cdot CN \cdot x_{metallic\ Ir}$$

Eq. S8

$$S^2_{0,rutile\ IrO_2} = amp_{rutile\ IrO_2} \cdot CN \cdot (1 - \ x_{metallic\ Ir})$$

where the 'amp_i' values was set to the respective S_0^2 factors (obtained by fits of the Ir^0 and rutile-IrO_2 standards by their respective structures, see **Table S7**), the CN values were fixed by their respective values for each shell of the elemental Ir and rutile-IrO_2 structures, and $x_{metallic\ Ir}$ was unconstrained.

Figure S14 shows the fitted Ir L_3-edge EXAFS and FT spectra of HIROF grown up to 1000 cycles. The bond lengths and Debye-Waller factors obtained from the EXAFS fits are given in **Table S3**.

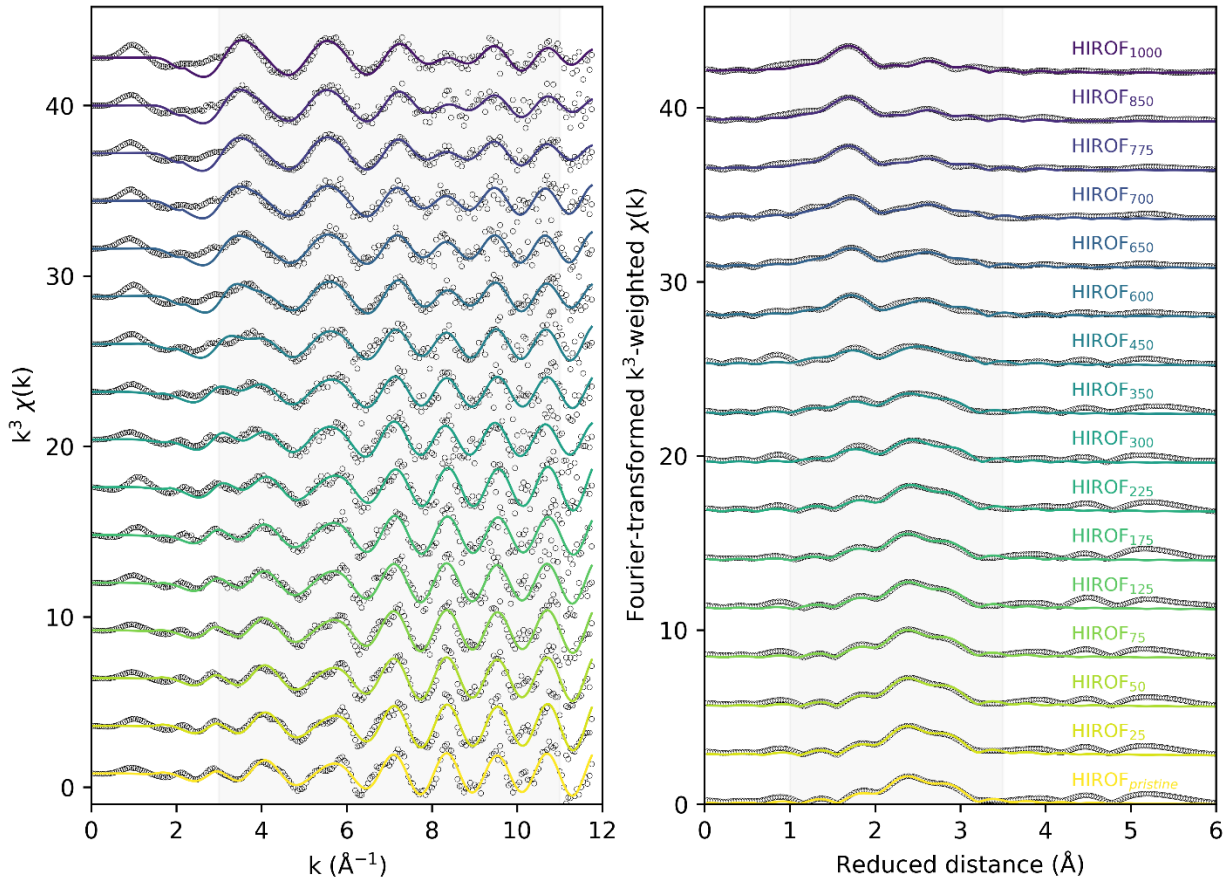

Figure S14. *a) k^3-weighted Ir L_3-edge EXAFS spectra and b) Fourier transformed k^3-weighted spectra of HIROF during its growth from a metallic Ir substrate up to 1000 cycles. The experimental (open circles) and fits (solid lines) are shown. The EXAFS fitting was done using rutile-IrO_2 and Ir^0 structures and fitting over the region k = 3 – 11 $Å^{-1}$ and R = 1 – 3.5 Å using the first shells from each structure.*

***Table S3**. Fit parameters for the Ir L_3-edge EXAFS data of HIROF during its growth fitted with IrO_2 and Ir^0 structures for k = 3 – 11 $Å^{-1}$ over the range R = 1 – 3.5 Å.*

Sample	Shell	N	x	σ^2 ($Å^2$)	ΔE_0 (eV)	R (Å)	R-factor
$HIROF_{pristine}$	Ir-O	2		0.0007 ± 0.0204		1.86 ± 0.09	
	Ir-O	4	0.8 ± 0.12	0.0262 ± 0.0204	10.64 ± 1.49	1.89 ± 0.09	0.02
	Ir-Ir	12		0.0035 ± 0.001		2.72 ± 0.01	
$HIROF_{25}$	Ir-O	2		0.029 ± 0.0232		1.85 ± 0.11	
	Ir-O	4	0.79 ± 0.12	0.029 ± 0.0232	10.59 ± 1.54	1.88 ± 0.11	0.02
	Ir-Ir	12		0.003 ± 0.0011		2.71 ± 0.01	
$HIROF_{50}$	Ir-O	2		0.0312 ± 0.0299		1.88 ± 0.14	
	Ir-O	4	0.81 ± 0.13	0.0312 ± 0.0299	10.44 ± 1.55	1.92 ± 0.14	0.02
	Ir-Ir	12		0.0034 ± 0.0011		2.72 ± 0.01	
$HIROF_{75}$	Ir-O	2		0.0584 ± 0.0216		1.94 ± 0.09	
	Ir-O	4	0.07 ± 0.01	0.0584 ± 0.0216	10.43 ± 1.63	1.97 ± 0.09	0.02
	Ir-Ir	12		0.0035 ± 0.0011		2.71 ± 0.01	
$HIROF_{125}$	Ir-O	2		0.051 ± 0.0182		1.96 ± 0.08	
	Ir-O	4	0.07 ± 0.01	0.051 ± 0.0182	10.98 ± 1.95	1.99 ± 0.08	0.03
	Ir-Ir	12		0.0036 ± 0.0013		2.72 ± 0.01	
$HIROF_{175}$	Ir-O	2		0.0418 ± 0.0111		2.01 ± 0.05	
	Ir-O	4	0.07 ± 0.01	0.0418 ± 0.0111	10.71 ± 1.71	2.04 ± 0.05	0.03
	Ir-Ir	12		0.0044 ± 0.0012		2.71 ± 0.01	
$HIROF_{225}$	Ir-O	2		0.039 ± 0.0098		1.97 ± 0.05	
	Ir-O	4	0.06 ± 0.01	0.039 ± 0.0098	13.29 ± 1.96	2.01 ± 0.05	0.03
	Ir-Ir	12		0.003 ± 0.0013		2.72 ± 0.01	
$HIROF_{300}$	Ir-O	2		0.0282 ± 0.0086		2.00 ± 0.05	
	Ir-O	4	0.06 ± 0.02	0.0282 ± 0.0086	12.45 ± 3.22	2.03 ± 0.05	0.08
	Ir-Ir	12		0.0039 ± 0.0021		2.73 ± 0.01	
$HIROF_{350}$	Ir-O	2		0.0232 ± 0.0049		1.99 ± 0.03	
	Ir-O	4	0.06 ± 0.01	0.0232 ± 0.0049	10.88 ± 2.65	2.02 ± 0.03	0.05
	Ir-Ir	12		0.0043 ± 0.0017		2.71 ± 0.01	
$HIROF_{450}$	Ir-O	2		0.0209 ± 0.0055		1.99 ± 0.05	
	Ir-O	4	0.04 ± 0.02	0.0209 ± 0.0055	12.73 ± 4.29	2.02 ± 0.05	0.10
	Ir-Ir	12		0.0026 ± 0.0025		2.73 ± 0.02	
$HIROF_{600}$	Ir-O	2		0.0105 ± 0.0023		2.03 ± 0.03	
	Ir-O	4	0.04 ± 0.01	0.0105 ± 0.0023	17.67 ± 2.68	2.07 ± 0.03	0.07
	Ir-Ir	12		0.0032 ± 0.0024		2.74 ± 0.01	
$HIROF_{650}$	Ir-O	2		0.0109 ± 0.0019		2.03 ± 0.02	
	Ir-O	4	0.03 ± 0.01	0.0109 ± 0.0019	17.12 ± 2.38	2.07 ± 0.02	0.04
	Ir-Ir	12		0.0023 ± 0.002		2.75 ± 0.01	

***Table S3**. Continued.*

Sample	Shell	N	x	σ^2 (Å^2)	ΔE_0 (eV)	R (Å)	R-factor
$HIROF_{700}$	Ir-O	2		0.0049 ± 0.0018		2.03 ± 0.02	
	Ir-O	4	0.27 ± 0.07	0.0049 ± 0.0018	17.69 ± 1.93	2.06 ± 0.02	0.03
	Ir-Ir	12		0.0006 ± 0.0018		2.75 ± 0.01	
$HIROF_{775}$	Ir-O	2		0.0029 ± 0.0013		2.03 ± 0.01	
	Ir-O	4	0.28 ± 0.06	0.0029 ± 0.0013	17.59 ± 1.41	2.06 ± 0.01	0.02
	Ir-Ir	12		0.0025 ± 0.0016		2.75 ± 0.01	
$HIROF_{850}$	Ir-O	2		0.0032 ± 0.0016		2.03 ± 0.01	
	Ir-O	4	0.27 ± 0.08	0.0032 ± 0.0016	18.21 ± 1.73	2.07 ± 0.01	0.03
	Ir-Ir	12		0.0028 ± 0.0021		2.75 ± 0.01	
$HIROF_{1000}$	Ir-O	2		0.0027 ± 0.0014		2.03 ± 0.01	
	Ir-O	4	0.22 ± 0.07	0.0027 ± 0.0014	18.57 ± 1.57	2.06 ± 0.01	0.03
	Ir-Ir	12		0.0013 ± 0.0023		2.75 ± 0.01	

The Debye-Waller (σ) parameters, energy shift (ΔE_0) and coordination distances (R) were unconstrained.

The coordination numbers (N) were kept as in the crystal structures: fcc metallic Ir and rutile IrO_2.

The passive electron reduction factor (S_0^2) was determined from the Ir^0 and IrO_2 references and set to be 0.78 ± 0.12 for the metallic Ir and 0.83 ± 0.15 for rutile IrO_2 structural model to approximate the am-hydr-IrOx component in HIROF.

S6.2. Comparison of the determined mole fractions and EXAFS fitting r-factors for different atomistic structures used to model am-hydr-IrO_x

Figure S15a shows the change in the molar fraction of the am-hydr-IrO_x component in HIROF as modelled using the rutile-IrO_2 structure. These EXAFS fits to determine the molar fraction of am-hydr-IrO_x were repeated using different structural models: the best fitting atomic model (H-terminated nanosheet Θ_H = 0.50 ML) and its version with more periodic nature (H-terminated stacked nanosheet) and thus lower H_2O intercalation volume. These atomic models and their elucidation is described later in **Supplementary Note 12** and in the main text of the manuscript.

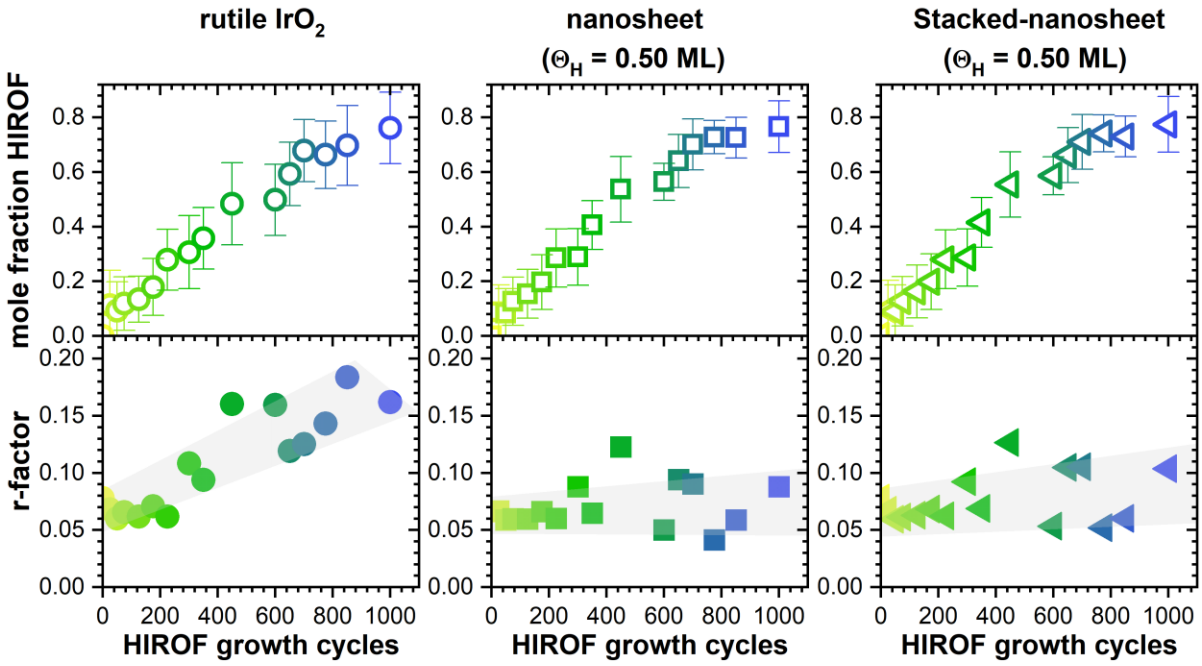

Figure S15. *Mole fraction of am-hydr-IrO_x species in HIROF and r-factor as determined by EXAFS fits using the first shell scattering paths of the Ir^0 and a) IrO_2, b) Sheet Θ_H = 0.50 ML and c) Stacked sheets Θ_H = 0.50 ML structures. The grey regions depict the general trend of the r-factor with growth cycles.*

It is clear that using the nanosheet and stacked nanosheet structures of iridium oxide with Θ_H = 0.50 ML results in an overall better EXAFS fits than using rutile-IrO_2 structure (i.e., lower r-factors as shown in the bottom panels in **Figure S15**). The r-factor for the fits using the nanosheet structure (Θ_H = 0.50 ML) consistently remains low ($\text{r-factor}_{\text{average}}$ = 0.07 ± 0.05) across all growth cycles. Whereas, as the quantity of am-hydr-IrO_x increases in the sample environment with increasing growth cycles (top panels in **Figure S15**), the discrepancy between the experimental data and the ability of the rutile-IrO_2 atomistic model to describe it grows. This is reflected in the poorer EXAFS fits when using rutile-IrO_2 (i.e., larger r-factor values, up to 0.18 with increasing growth cycles 1000 cycles). The more consistent and lower r-factor values as a function of growth cycles when using nanosheet structure indicate that this atomic model is a better descriptor for am-hydr-IrO_x during its electrochemical growth from the metallic Ir

substrate. Furthermore, the mole fraction trend for am-hydr-IrO_x as a function of growth cycles obtained when using the nanosheet structure (Θ_H = 0.50 ML) correlates very well with the trend obtained when using the rutile-IrO_2 structure, affirming the robustness of our approach and reliability of the EXAFS data analysis.

Supplementary Note 7. *Theoretical analysis of the atomistic model structure of am-hydr-IrO_x*

S7.1. EXAFS evaluation procedure and atomistic model elimination approach

To elucidate the structure of am-hydr-IrO_x in HIROF, Ir L_3-edge EXAFS fits were performed using a two-component structural model, where the parameters of the metallic Ir scattering pathway were fixed according to the results presented in the **Supplementary Note 6** (i.e., *R*, *CN*, and the mole fraction = 0.2 ± 0.1). Individual fits were performed where the atomic model used to fit the am-hydr-IrO_x component in HIROF was systematically selected from the library of possible structures. In the fit model, all oxygen scattering paths within the first coordination shells were incorporated. The parameters *CNs* and *R* for these paths were held constant, while only the ΔE_0 and σ parameters were allowed to vary during the fitting procedure. The Larch software package[25] was used to execute the multiple EXAFS fits, and the *ab initio* atomic scattering paths were constructed using the FEFF 8.0 code[34].

Not only were EXAFS fits done using the two-component model (*fcc*-elemental Ir and an iridium oxide atomic model from the library), but adaptations to the number of scattering paths of the iridium oxide atomic model included in the fit were also explored. EXAFS fits were done either including or excluding the second coordination shell Ir-Ir scattering of the iridium oxide atomic model, which strongly overlaps with the first coordination shell Ir^0-Ir^0 scattering of the metallic Ir substrate in the FT spectra region 2 – 3.5 Å. Inclusion or exclusion of the second scattering path did not result in significantly different χ^2-values indicating that the inclusion of the additional scattering path does not affect the overall outcome of the goodness of fit of the EXAFS fits. This also therefore does not affect the outcome of which atomic models best fit the experimental data, and so EXAFS fits using only the first coordination shell scattering paths of the metallic Ir and iridium oxide atomic models presented in this work. The exclusion of structural options was made based on poor EXAFS refinement parameters such as large r-factor values, large ΔE_0 shifts and negative σ values. **Figure S16** shows a summary of the atomic model families and surface termination types (and coverages Θ_i which vary between 0 and 1 MLs) investigated within this study.

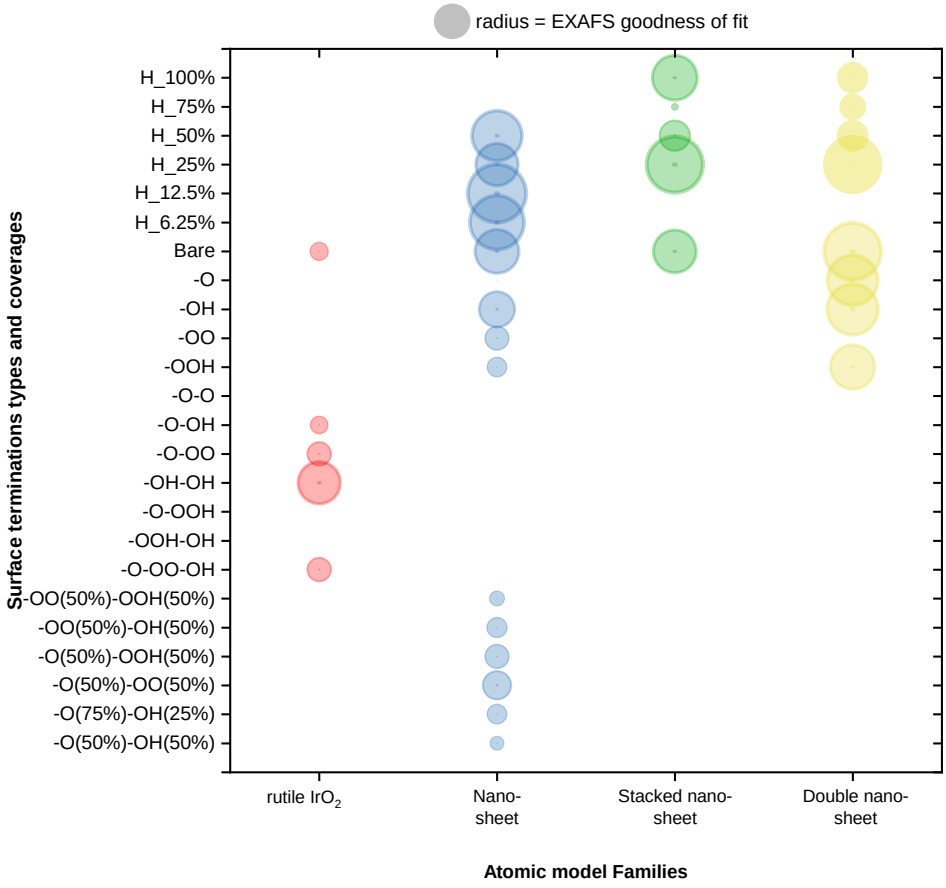

Figure S16. *EXAFS fits using all atomic models and surface termination types DFT eliminations of structural options to model HIROF. The EXAFS fit quality is given by the data point size which is equivalent to the inverse of the r-factor of the EXAFS fit.*

S7.2. Nanosheet structures best describing the elongated Ir-O bond in am-hydr-IrO_x

The best atomistic family derived from this process of evaluation of the experimental EXAFS data of am-hydr-IrO_x was single nanosheet structures with H-coverage. **Figure S17** below depicts these nanosheet atomistic models with varying H-coverage.

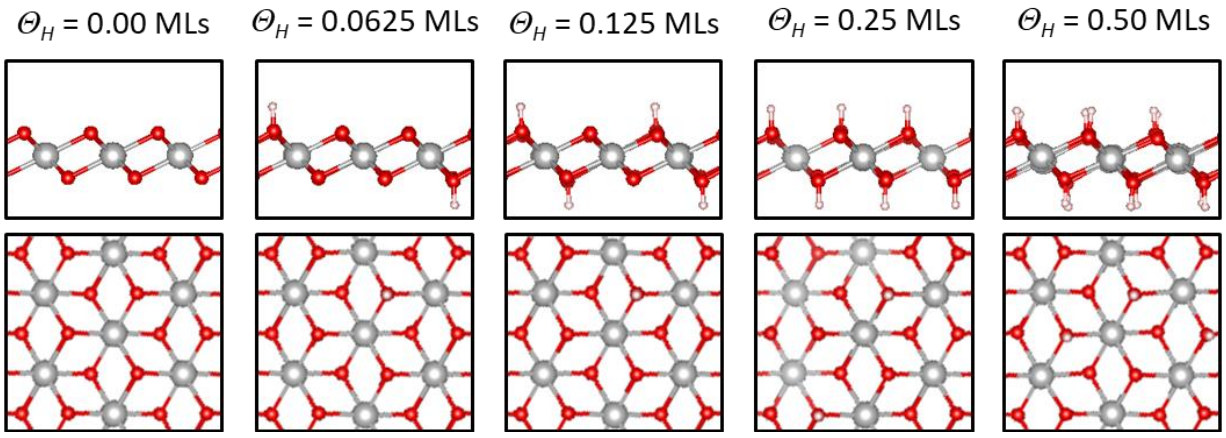

Figure S17. *Perspective views of the symmetric nanosheet slab structures with H-coverage (Θ_H = 0 – 0.50 ML). The grey spheres denote Ir atoms, red spheres O atoms, and white spheres H atoms.*

Supplementary Note 8. *Partial Density of States calculations*

Figure S18 shows the density of states (DOS) of all the most stable structures according to the phase diagram calculations presented in **Fig. 4a** and **b**. The Ir and O valence states overlap, which are related to hybridization of the orbitals and typically affect the catalytical activity.

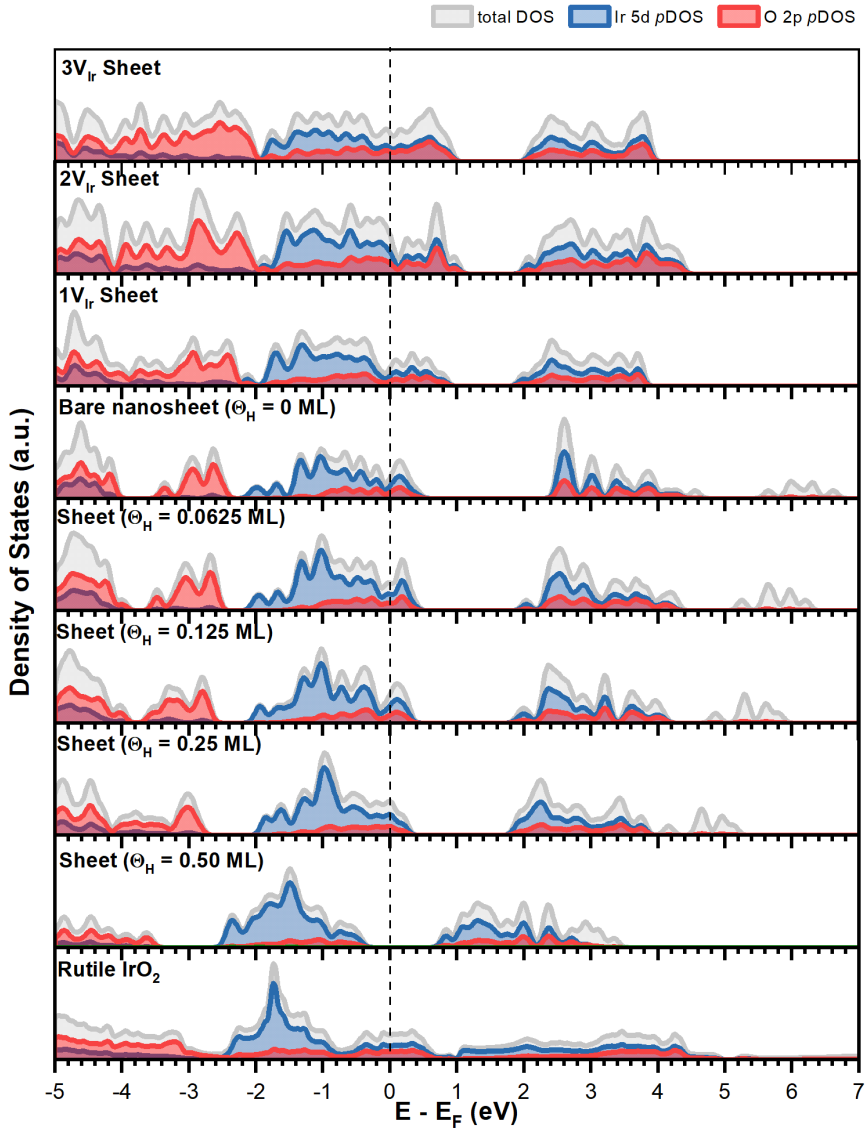

Figure S18. *Density of states (DOS) of the most stable structures as defined in the phase diagram: Sheet (Θ_H = 0.50, 0.25, 0.125, 0.0625 and 0 ML), 1V$_{Ir}$ sheet, 2V$_{Ir}$ sheet and for comparison rutile-IrO$_2$. The grey represents the total DOS. The partial density of states (pDOS) of the Ir 5d and O 2p orbitals are presented by the blue and red respectively. The Fermi energy is set to zero and is indicated by the vertical dashed line.*

The Ir:O:H stoichiometry ratios of these most stable structures are shown **Figure S18** are summarized in **Table S4** below:

Table S4. *Stoichiometry (Ir:O:H) of the most thermodynamically stable nanosheet structures as shown in* ***Figure S18****.*

Structure	**Ir:O:H stoichiometry**
Rutile-IrO_2	1:2:0
Nanosheet (θ = 0.50 ML)	1:2:1
Nanosheet (θ = 0.25 ML)	2:4:1
Nanosheet (θ = 0.125 ML)	4:8:1
Nanosheet (θ = 0.0625 ML)	8:16:1
Bare nanosheet (θ = 0 ML)	1:2:0
1 V_{Ir} nanosheet	15:32:0
2 V_{Ir} nanosheet	7:16:0
3 V_{Ir} nanosheet	13:32:0

To understand the correlation between the formal oxidation states and the calculated electronic structure of active sites, we tabulate the formal average oxidation states derived from a simple electron-counting method, alongside the corresponding Bader charges for key iridium sites, in **Table S5**. While formal oxidation states are typically represented as integers, systems with delocalized bonding or n-fold coordination can be more accurately described using formal average oxidation states. These states reflect the shared electronic environment across multiple atoms, resulting in non-integer values. For instance, the iridium atom at the sheet surface with an oxygen vacancy (denoted as * of sheet surface O model) is coordinated by five oxygen atoms, each of which is coordinated to three iridium atoms. This results in a formal average oxidation state for the Ir atom of $\frac{2+}{3} \times 5 = 3.33+$.

Notably, the geometry optimization of the –OOH group in the $2V_{Ir}$ and edge models reveals proton transfer from –OOH to the neighbouring –O, forming –OO and –OH groups. Consequently, the oxidation states and Bader charges for both iridium atoms adjacent to these –OO and –OH are provided in **Table S5**.

Table S5. *Formal average oxidation states (O.S.) and Bader charge (q_{Bader}) analysis for Ir atoms associated with various reaction intermediates at the active sites. In the $2V_{Ir}$ and edge models, the –OOH group undergoes proton transfer to the neighbouring –O, resulting in the formation of –OO and –OH groups. The corresponding O.S. and q_{Bader} values for both Ir atoms bound to these –OO and –OH groups are provided, respectively.*

Reaction coordinate	Sheet surface O^{3f}		Sheet surface Ir^{6f}		$1V_{Ir}$		$2V_{Ir}$		Edge	
	O.S.	q_{Bader}	O.S.	q_{Bader}	O.S.	q_{Bader}	O.S.	q_{Bader}	O.S.	q_{Bader}
*	3.33	1.21	4	1.57	3.67	1.36	4	1.65	4	1.59
*-O	4	1.57	6	1.80	4.67	1.68	6	1.90	6	1.74
*-OH	3.67	1.52	5	1.73	4.17	1.64	5	1.78	5	1.72
*-OOH	3.67	1.49	5	1.67	4.17	1.62	6 / 5	1.70/ 1.78	6 / 5	1.69/ 1.83

The electron density analysis of the edge model's –OO…H–O– moiety reveals significant electron density between the –OO and hydrogen, with the majority concentrated around the H–O bond, as shown in **Figure S19a**, illustrating a slice along the 2D plane centred on the O-O and H atoms. The potential energy surface scan shown in **Figure S19b** confirms a shallow double minimum potential for hydrogen transfer between the –OO and –OH groups, with a small energy barrier of approximately 0.16 eV. This observation indicates a partially covalent bond between these sites.

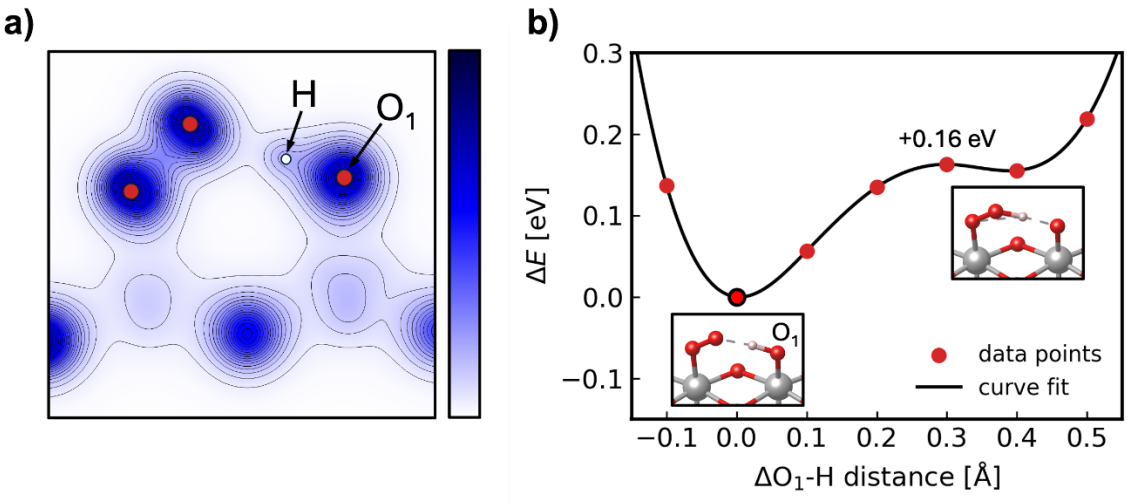

Figure S19. a) *Electron density plot showing the distribution between the terminal oxygen atoms of the –OO…H…O– moiety of the edge model.* ***b)*** *The shallow double minimum potential energy profile for hydrogen transfer between the –OO and –O groups in the edge structure.*

Therefore, a simple electron-counting approach, where oxidation states of 6+ and 5+ are assigned to the iridium atoms bound to –OO and –OH groups, respectively, reveals a notable

discrepancy compared to Bader charge results (as shown in **Figure S20a**). A more straightforward approximation involves assuming an –[OO]$^-$ moiety hydrogen-bonded to a neighbouring –OH, resulting in identical oxidation states for the involved Ir atoms. This approach aligns well with the Bader charge analysis for the symmetric $2V_{Ir}$ configuration:

[Ir–OO$^-$…H–O–Ir] ↔ [Ir–OO–H…$^-$O–Ir]

where all iridium atoms exhibit partial charges in the range of 1.7-1.8, corresponding to a formal oxidation state of 5+.

However, this approximation might be overly simplistic for accurately capturing the true electronic structure of the motif, which is better described as a fluxional [Ir–O–O$^{\delta-}$…H$^{\delta+}$–O–Ir]. In this context, assigning an average fractional oxidation state of 5.5+ to each iridium atom yields a better correlation between the formal oxidation states and the computed Bader charges for the edge case, as shown in **Figure S20b**. Nonetheless, this approach does not completely resolve the discrepancy, *i.e.*, the reversal of ordering between the Ir sites in the edge model in **Table S5**, between formal electron counting and Bader analysis results.

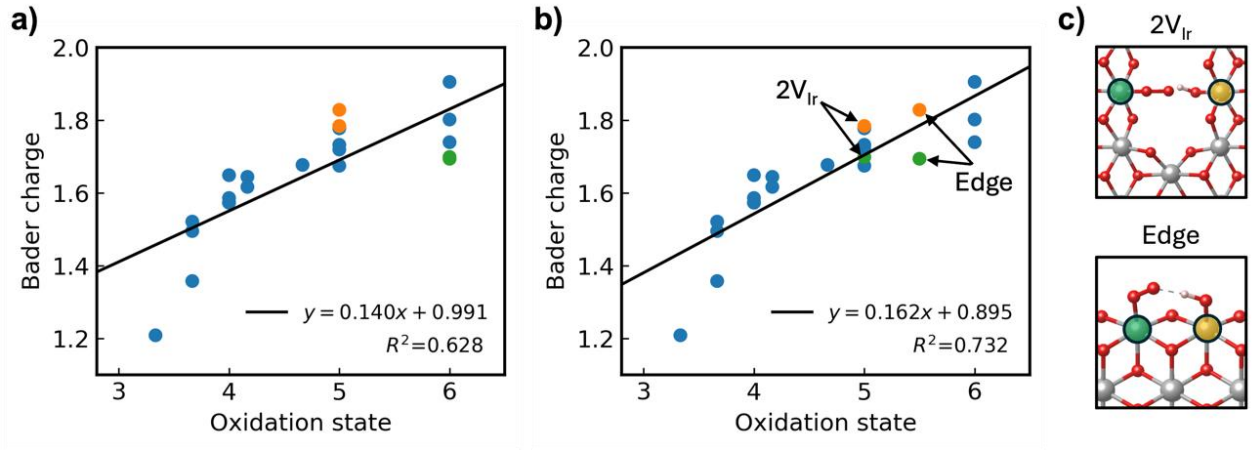

Figure S20. a) *Correlation plot between the formal oxidation state derived from simple electron-counting and the Bader charge of Ir atoms. The linear fit function and R^2 factor are annotated in the inset. Green and orange scatter points represent Ir atoms ($2V_{Ir}$ and edge sites) with –OO and –OH groups, respectively.* ***b)*** *The same correlation plot, adjusted for the oxidation states of two Ir atoms in the Ir–OO…H…O–Ir moiety for the $2V_{Ir}$ and edge models.* ***c)*** *Local atomic structures of the $2V_{Ir}$ and edge models, highlighting the Ir sites with –OO (green) and –OH (yellow).*

Supplementary Note 9. *Ir-O bond distributions of atomistic models*

S8.1. Determination of the Ir-O bond distributions of the atomistic models

The Ir-O bond distributions of the different atomistic models depicted in the phase diagram in **Figure 5** of the main text (the Ir^{6f}, $1V_{Ir}$, $2V_{Ir}$ and edge site OER pathways) were analyzed using the Atoms format of Atomic Simulation Environment (ASE)[35], and the raw data is presented using Origin as violin plots with bin sizes of 0.02 Å, a Scott bandwidth, and a smooth kernel curve type. The distribution of all the Ir-O bond lengths within the 2D nanosheet supercells (16 IrO_2 units) are presented in **Figure S21**.

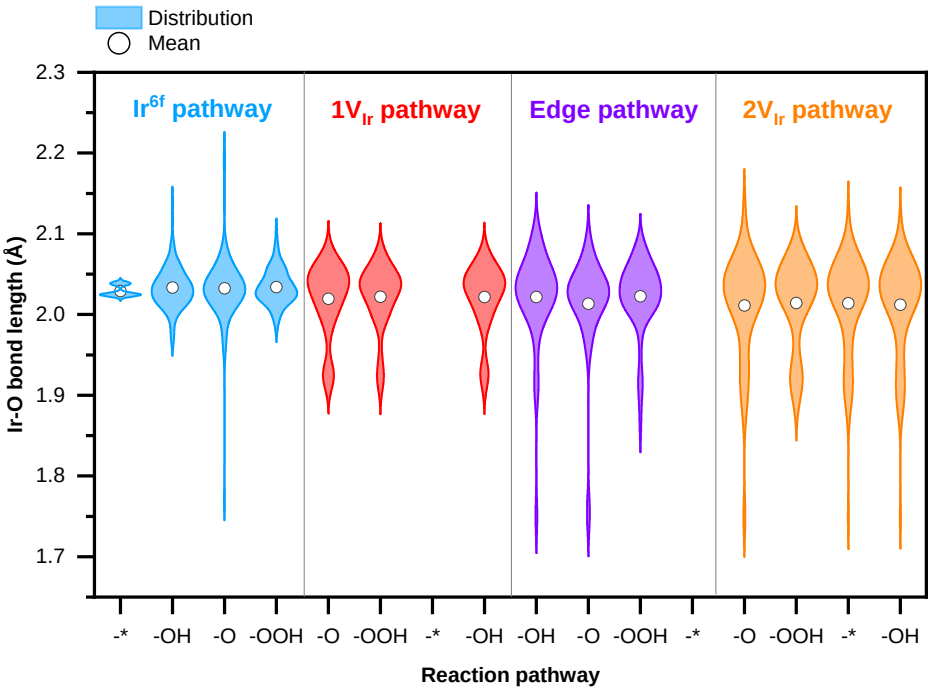

Figure S21. *Ir-O bond distance distributions of the nanosheet atomistic structures with terminations at the sheet surface Ir^{6f} (in blue), $1V_{Ir}$ (in red), sheet edge (in purple), and $2V_{Ir}$ (in orange) sites. The mean Ir-O bond distances are shown as open white circles.*

S8.2. Analysis of the distribution of the Ir-O bond lengths

As the perturbation to the bare nanosheet (either *, *O, *OH, or *OOH configurations) is only performed to one IrO_2 unit within the supercell (coverage of 0.03125 MLs), the distribution of all the Ir-O bond lengths includes (1) strain effects at the central Ir atom where the perturbation occurs, (2) strain/relaxation effects in the second coordination shell supporting the central Ir atom, (3) strain/relaxation effects in the third coordination shell supporting the central Ir atom, and lastly (4) edge site effects (see **Figure S22** for a ball-stick perspective view).

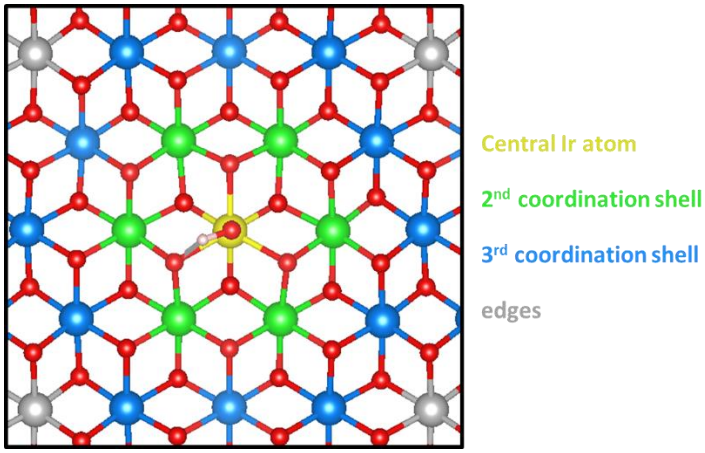

Figure S22. *Perspective view of atomistic model Ir^{6f}*O where *O is adsorbed on the central Ir atom (in yellow). The 2nd coordination shell Ir atoms are shown in green, the 3rd coordination shell iridium atoms are shown in blue and the iridium atoms on the edge sites are shown in grey.*

There is an exponential decrease in the strain/relaxation effects radiating away from the central perturbated Ir atom. This can be demonstrated by the diminishing broadness in the Ir-O bond length distributions with increasing coordination shells away from the central Ir atom, in the example case of *O on an Ir^{6f} site shown in **Figure S23**.

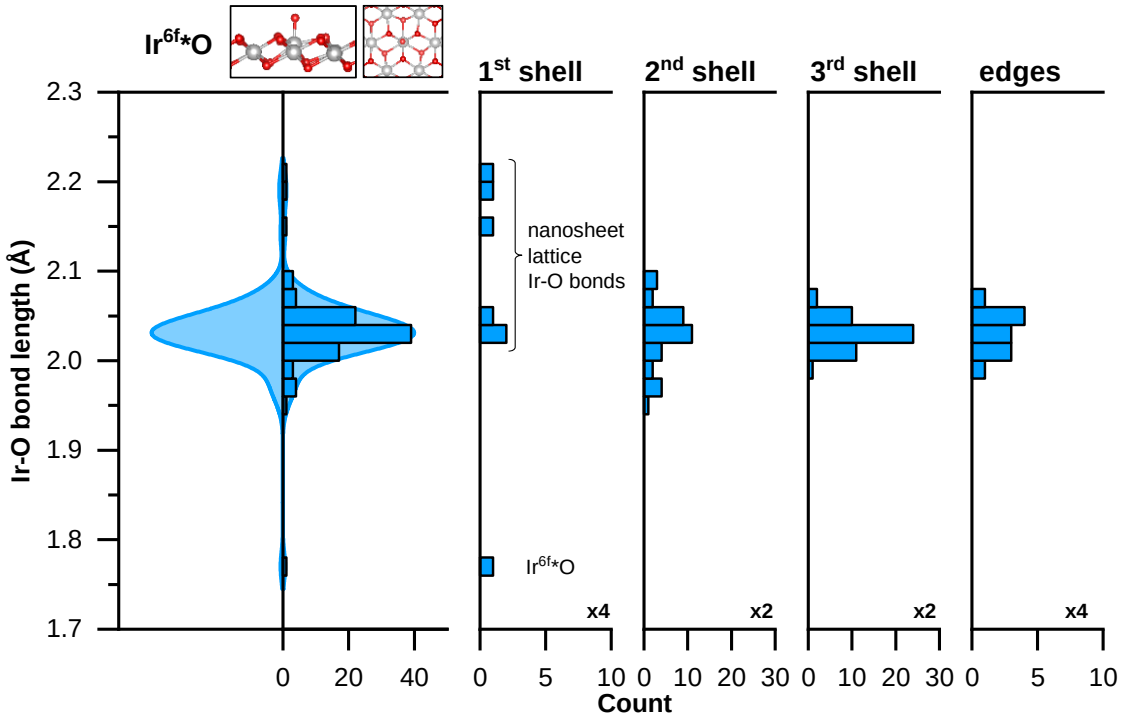

Figure S23. *Ir-O bond distance distributions of the 2D nanosheet atomistic structure Ir^{6f}*O (coverage of 0.03125 ML of *O). The left violin plot and histogram depicts the entire Ir-O bond length distributions of the 16 IrO_2 unit supercell. The subplots depict the Ir-O bonds only associated with the 1st, 2nd, and 3rd coordinations shells, and edges. Where the perturbation of the *O adsorbate occurs on the central Ir atom in the 1st coordination shell, the largest Ir-O bond length distribution is observed.*

Note, that these Ir-O distributions would be different for higher coverages since the strain and relaxation effects in the nanosheet would be distributed differently. This highlights the presence of shorter Ir-O bond lengths to the *O, *OH, and *OOH sites as shown in **Figure 4d**.

Similarly, the Ir-O bond length distributions around Ir defect sites were analysed. **Figure S37** shows the distributions of Ir-O bond lengths in the $1V_{Ir}$ nanosheet atomistic model, where the shortest bond lengths arise around the Ir defect site.

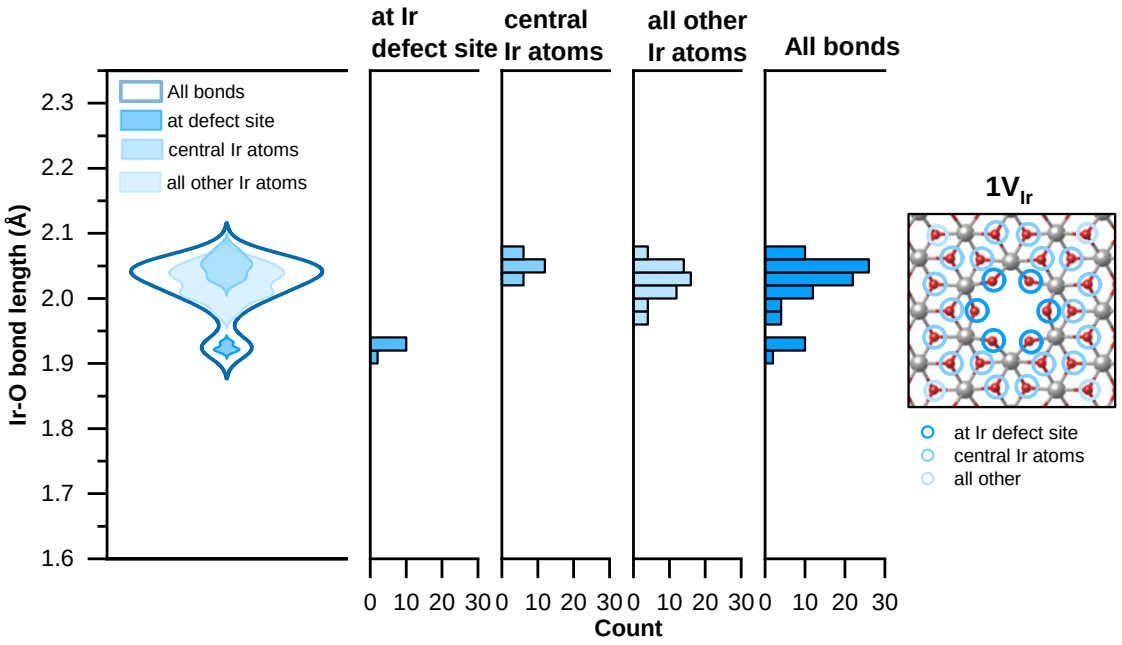

Figure S24. *Ir-O bond distance distributions of the 2D nanosheet atomistic structure $1V_{Ir}$. The left violin plots depicts the all the Ir-O bond lengths around the Ir defect site in the 16 IrO_2 unit supercell. The subplots to the right depict the Ir-O bonds only associated around the Ir defect site, the central Ir atoms, and all other Ir atoms at the sheet edges. The shortest Ir-O bond lengths are observed around the Ir defect site.*

Supplementary Note 10. *Ab initio thermodynamic analysis*

S10.1. Comparison of Ir and O vacancy formation in the nanosheet model

Comparison of the DFT-predicted stability of nanosheets with oxygen vacancies versus iridium vacancies is shown in **Figure S25** below.

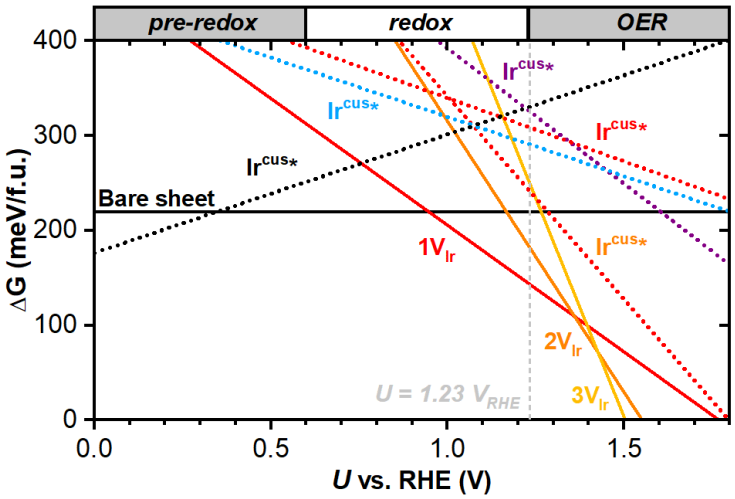

Figure S25. *Ab initio DFT calculations of the phase diagram showing the stability of different H-coverages on the O^{3f} sites of the nanosheet surface (shown in blue) and on the O^{2f} sites of the $1V_{Ir}$ nanosheet (shown in red) as a function of the applied potential U (vs RHE).*

S10.1. Evaluation of the DFT peroxide pathway on different sites in the nanosheet model

Figure S26 to **Figure S30** show the four electron-transfer steps and associated Gibbs free energy change for the classic DFT peroxide pathway[36] on the most stable structures (as given by the phase diagram **Figure 4** in the main text), starting from their resting states, which are the most-phase-diagram stable intermediates at the ideal onset of 1.23 V. However, the resting state can shift depending on the overpotential, and it is not always the empty active site. For comparison, the phase diagram the different terminations which represent the intermediate states in the OER pathway is also shown.

These calculations refer to asymmetric slab models with one termination species in the supercell structure yield 0.03125 ML coverages, where dipole corrections are applied to mitigate the energetic and force errors from the broken symmetries at upper and lower slabs.

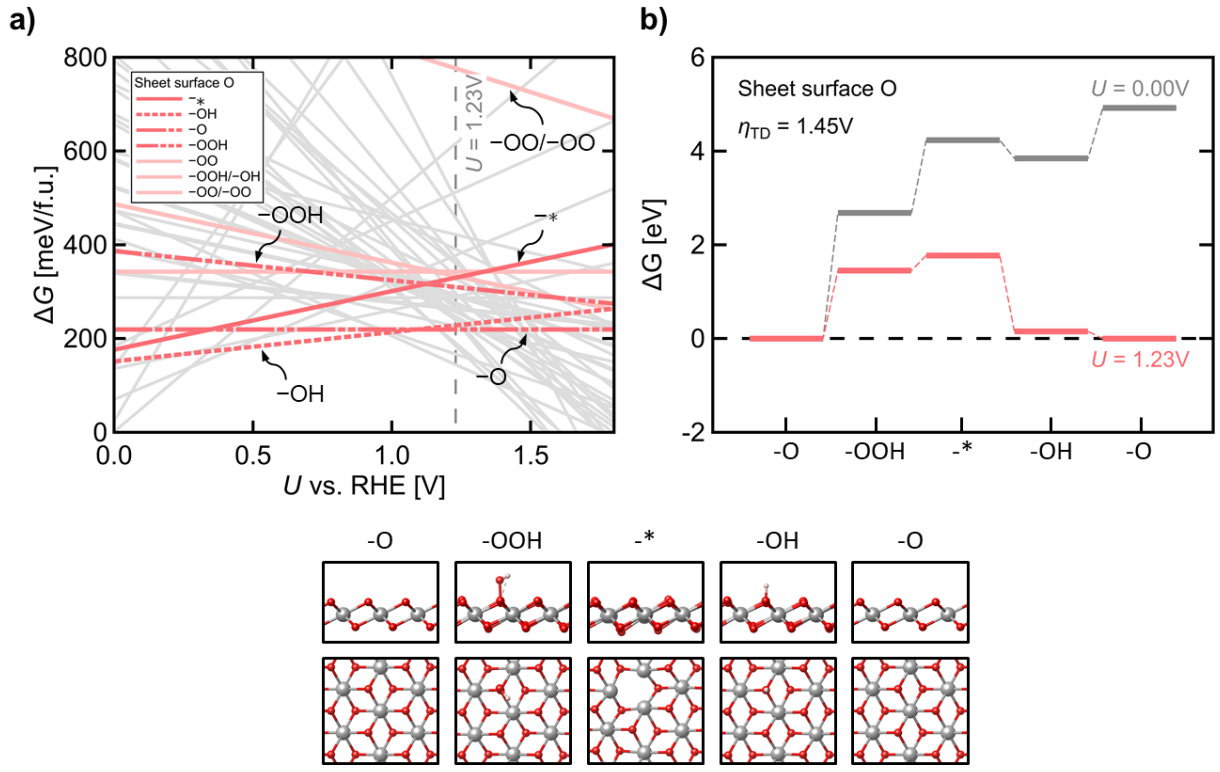

Figure S26. *Ab initio DFT calculations of a) the phase diagram showing the stability of different terminations of the sheet surface as a function of the applied potential U (vs RHE) which represent all the intermediates in the b) the computed reaction energy changes along the classic DFT peroxide OER pathway for the O-site on the pristine sheet (Θ_H = 0 ML) starting from the resting state (*O).*

In the case of **Figure S26**, which illustrates the classic DFT peroxide pathway[36] on the O^{3f} surface sites, the labelled *O, *OOH, *, and *OH species refer to $*O^{1f}$, $*O^{1f}$-OH, $[Ir^{cus/5f}]*$, $*O^{1f}$-H species, respectively, in the nanosheet atomistic structure. $[Ir^{cus/5f}]*$ acts as the underlying functional

active site. The same nomenclature is used in the main text discussion of **Fig. 4** and **5**. The reaction steps are as follows:

1. $*O^{3f} + H_2O \rightarrow *O^{3f}\text{-}OH + H^+ + e^-$
2. $*O^{3f}\text{-}OH \rightarrow [Ir^{cus/5f}]* + O_2 + H^+ + e^-$
3. $[Ir^{cus/5f}]* + H_2O \rightarrow *O^{3f}\text{-}H + H^+ + e^-$
4. $*O^{3f}\text{-}H \rightarrow *O^{3f} + H^+ + e^-$

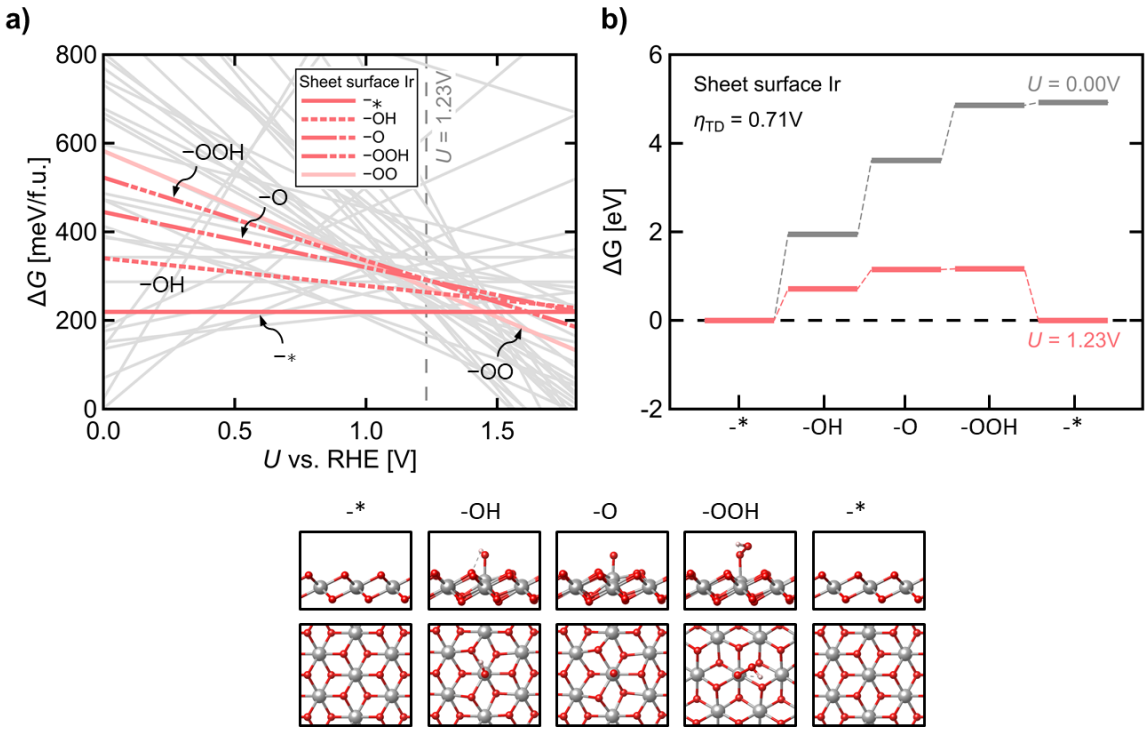

Figure S27. *Ab initio DFT calculations of a) the phase diagram showing the stability of different terminations of the sheet surface as a function of the applied potential U (vs RHE) which represent all the intermediates in the b) the computed reaction energy changes along the classic DFT peroxide OER pathway for the Ir-site on the pristine sheet (Θ_H = 0 ML) starting from the resting state (-*).*

In the case of **Figure S27**, which illustrates the classic DFT peroxide pathway[36] on the Ir^{6f} surface sites, the labelled *, *OH, *O, and *OOH species refer to $*Ir^{6f}$, $*Ir^{6f}\text{-}OH$, $*Ir^{6f}\text{-}O$, and $*Ir^{6f}\text{-}OOH$ species, respectively, in the nanosheet atomistic structure. The same nomenclature is used in the main text discussion of **Fig. 4** and **5**. The reaction steps are as follows:

1. $*Ir^{6f} + H_2O \rightarrow *Ir^{6f}\text{-}OH + H^+ + e^-$
2. $*Ir^{6f}\text{-}OH \rightarrow *Ir^{6f}\text{-}O + H^+ + e^-$
3. $*Ir^{6f}\text{-}O + H_2O \rightarrow *Ir^{6f}\text{-}OOH + H^+ + e^-$
4. $*Ir^{6f}\text{-}OOH \rightarrow O_2 + H^+ + e^-$

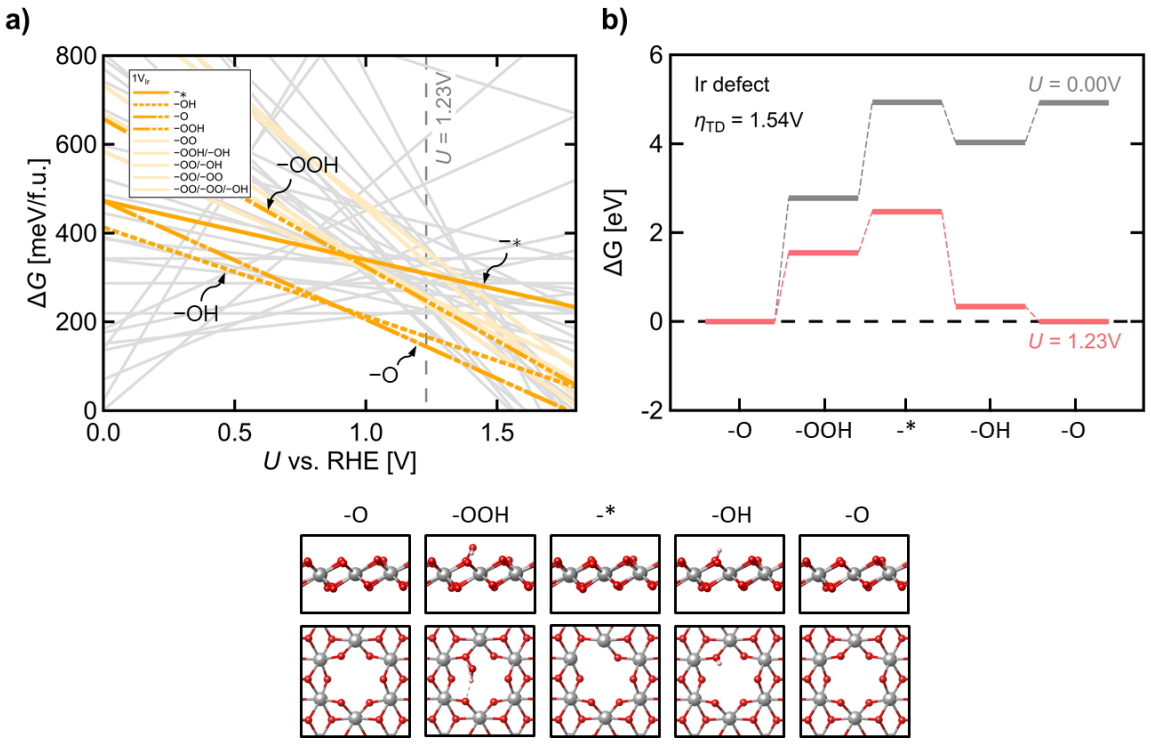

Figure S28. *Ab initio DFT calculations of a) the phase diagram showing the stability of different terminations of the sheet surface as a function of the applied potential U (vs RHE) which represents all the intermediates in the b) the computed reaction energy changes along the classic DFT peroxide OER pathway of the defect site in the $1V_{Ir}$ sheet starting from the resting state (*O).*

In the case of **Figure S28**, which illustrates the classic DFT peroxide pathway[36] on the O^{2f} sites in the $1V_{Ir}$ structure, the labelled *O, *OOH, *, and *OH species refer to $*O^{2f}$, $*O^{2f}$-OH, $[Ir^{cus/5f}]*$ and $*O^{2f}$-O species, respectively, in the nanosheet atomistic structure. $[Ir^{cus/5f}]*$ acts as the underlying functional active site. The same nomenclature is used in the main text discussion of **Fig. 4** and **5**. The reaction steps are as follows:

1. $*O^{2f} + H_2O \rightarrow *O^{2f}\text{-}OH + H^+ + e^-$
2. $*O^{2f}\text{-}OH \rightarrow [Ir^{cus/5f}]* + O_2 + H^+ + e^-$
3. $[Ir^{cus/5f}]* + H_2O \rightarrow *O^{2f}\text{-}H + H^+ + e^-$
4. $*O^{2f}\text{-}H \rightarrow *O^{2f} + H^+ + e^-$

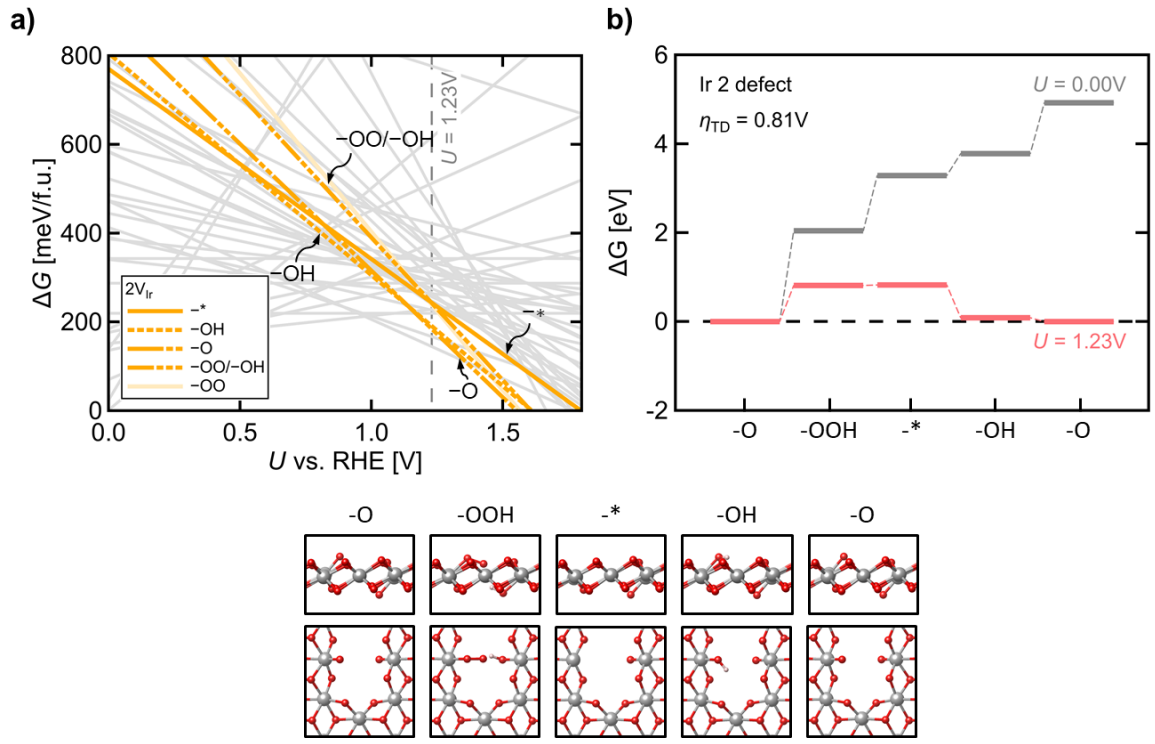

Figure S29. *Ab initio DFT calculations of a) the phase diagram showing the stability of different terminations of the sheet surface as a function of the applied potential U (vs RHE) which represent all the intermediates in the b) the computed reaction energy changes along the classic DFT peroxide OER pathway of the defect site in the $2V_{Ir}$ sheet starting from the resting state (*O).*

In the case of **Figure S29**, which illustrates the classic DFT peroxide pathway[36] on the O^{1f} sites in the $2V_{Ir}$ structure, the labelled *O, *OOH, *, and *OH species refer to $*O^{1f}$, $*O^{1f}$-OH, $[Ir^{cus/5f}]*$ and $*O^{1f}$-O species, respectively, in the nanosheet atomistic structure. $[Ir^{cus/5f}]*$ acts as the underlying functional active site. The same nomenclature is used in the main text discussion of **Fig. 4** and **5**. The reaction steps are as follows:

1. $*O^{1f} + H_2O \rightarrow *O^{1f}\text{-}OH + H^+ + e^-$
2. $*O^{1f}\text{-}OH \rightarrow [Ir^{cus/5f}]* + O_2 + H^+ + e^-$
3. $[Ir^{cus/5f}]* + H_2O \rightarrow *O^{1f}\text{-}H + H^+ + e^-$
4. $*O^{1f}\text{-}H \rightarrow *O^{1f} + H^+ + e^-$

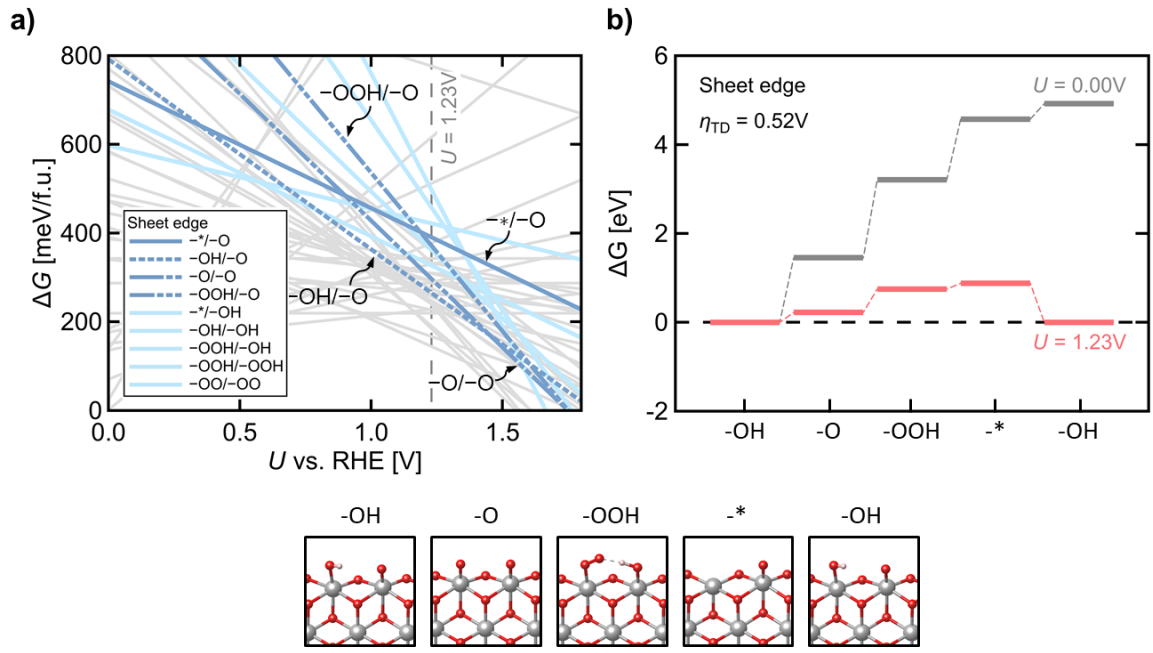

Figure S30. *Ab initio DFT calculations of a) the phase diagram showing the stability of different terminations of the sheet surface as a function of the applied potential U (vs RHE) which represent all the intermediates in the b) the computed reaction energy changes along the classic DFT peroxide OER pathway on the sheet edge starting from the resting state (*OH).*

In the case of **Figure S30**, which illustrates the classic DFT peroxide pathway[36] on the O^{cus} sites at the nanosheet edges, the labelled *OH, *O, *OOH, and * species refer to $*O^{cus}$-H, $*O^{cus}$, $*O^{cus}$-OH, and $[Ir^{5f}]*$ species, respectively, in the nanosheet atomistic structure. $[Ir^{cus/5f}]*$ acts as the underlying functional active site. The same nomenclature is used in the main text discussion of **Figure 4** and **5**.

The reaction steps are as follows:

1. $*O^{cus}\text{-}H \rightarrow *O^{cus} + H^+ + e^-$
2. $*O^{cus} + H_2O \rightarrow *O^{cus}\text{-}OH + H^+ + e^-$
3. $*O^{cus}\text{-}OH \rightarrow [Ir^{cus/5f}]* + O_2 + H^+ + e^-$
4. $[Ir^{cus/5f}]* + H_2O \rightarrow *O^{cus}\text{-}H + H^+ + e^-$

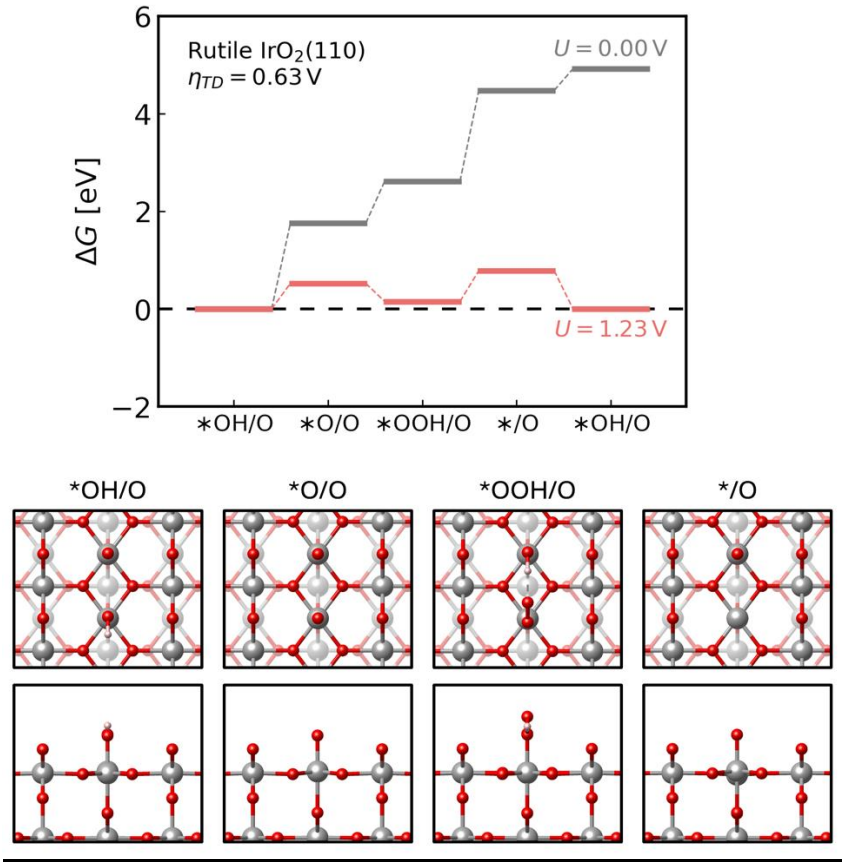

Figure S31. *The computed reaction energy changes along the classic DFT peroxide OER pathway for the Ir-site on the rutile IrO_2(110) starting from the resting state (*OH/O).*

It is important to note that the minimum thermodynamic overpotential derived from the computational hydrogen electrode approach is not directly comparable to the experimentally measured overpotential. Instead, it serves as a relative measure for comparing different active site models[37]. In this context, the rutile IrO_2(110) model exhibits a thermodynamic overpotential of 0.63 V as shown in **Figure S31**, following the reaction steps:

1. $*O^{cus}\text{-}H \rightarrow *O^{cus} + H^+ + e^-$
2. $*O^{cus} + H_2O \rightarrow *O^{cus}\text{-}OH + H^+ + e^-$
3. $*O^{cus}\text{-}OH \rightarrow [Ir^{cus/5f}]* + O_2 + H^+ + e^-$
4. $[Ir^{cus/5f}]* + H_2O \rightarrow *O^{cus}\text{-}H + H^+ + e^-$

This overpotential is approximately 0.11 V higher than that of the sheet edges in our computational framework (**Figure S30**). This highlights the sheet edges as highly active zones for the OER, though refined microkinetic studies are necessary to fully elucidate the underlying mechanisms[38–42].

S10.1. Deprotonation behaviour of the nanosheet model without and with one Ir vacancy

Symmetric slabs calculations are shown in **Figure S32** for the dehydrogenation processes on the nanosheet surfaces using a pristine nanosheet atomistic model and a nanosheet with one Ir vacancy. In addition, we note that only the Gibbs free energy of *O^{3f}-H ($\Theta_H = 0.03125$ ML) in a **Figure S32** (and **Fig. 4a)** is obtained from an asymmetric slab due to the limited size of the simulating supercell, while the Gibbs free energies of other lowest energy models are from symmetric slabs. This indicates that deprotonation of the O^{3f} sites occurs within the same potential region whether an Ir vacant site exists or not. Deprotonation behaviour of the O^{2f} sites at the Ir vacancy is discussed in **Fig. 4** in the main text.

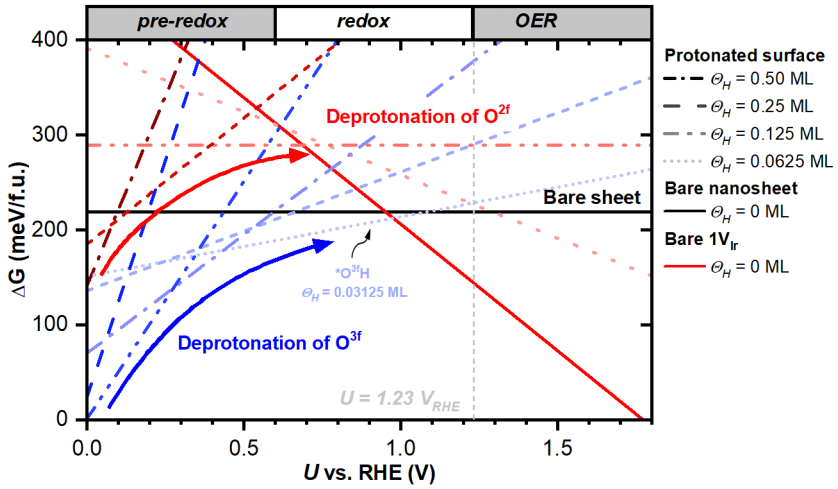

Figure S32. *Ab initio DFT calculations of the phase diagram showing the stability of different H-coverages on the O^{3f} sites of the nanosheet surface (shown in blue) and on the O^{2f} sites of the $1V_{Ir}$ nanosheet (shown in red) as a function of the applied potential U (vs RHE).*

Supplementary Note 11. *Preparation of the Ir^0 and IrO_2 thin film references*

Two thin films served as standards for OER activity and iridium oxidation states. Ir (99.9%, Evochem) and Ti (99.995%, FHR) targets of 2-inch diameter were pre-cleaned by sputtering against closed shutters before deposition. Both films followed a deposition process involving first the deposition of 5 nm Ti adhesion layer at 100 W on Si wafers with native SiO_2, before iridium deposition. The reference 30 nm Ir^0 thin film was prepared by DC magnetron sputtering at 50 W. For the reference 30 nm IrO_2 thin film, reactive magnetron sputtering at 50 W was employed using a mixture of O_2 and Ar as the sputtering gas. Subsequently, the IrO_2 thin film was annealed in air at 600°C for 2 hours to crystallize the film.

The metallic Ir substrates utilized for HIROF growth were prepared using similar conditions, with deposition times adjusted to achieve either 15 nm on Si wafers for *ex-situ* XPS characterizations or 25 nm on 8 µm thick Kapton film for *in situ* Ir L_3-edge XAS characterizations.

Supplementary Note 12. *Cryogenic Transmission Electron Microscopy (cryo-TEM)*

Due to the amorphous nature and dehydration caused by UHV conditions[3,13], cryogenic transmission electron microscopy (cryo-TEM) was used to image am-hydr-IrO_x in its native acidic hydrated state. Post preparation of HIROF, the am-hydro-IrO_x film was delaminated using ultra-sonication in 0.5 M H_2SO_4 for 10 min. The dispersed am-hydro-IrO_x in aqueous solution was drop-casted onto a lacey carbon carbon-coated copper TEM grid and plunge froze in liquid ethane at ~ -180°C. The cryogenic frozen hydrated state of am-hydro-IrO_x was imaged using an acceleration voltage of 200 keV.

Several thicker portions of the am-hydro-IrO_x films were observed, with several thinner sheets. Imaging of the amorphous porous structure was performed on the thinner am-hydro-IrO_x films.

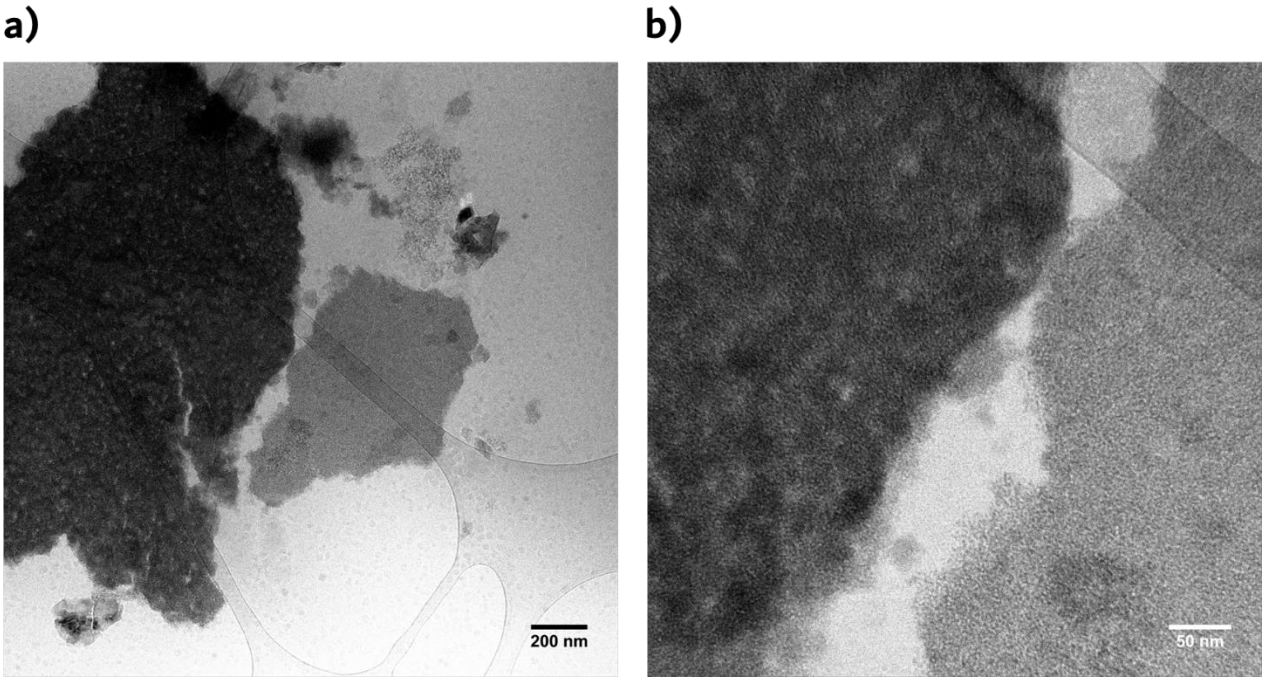

Figure S33*. Cryogenic Transmission Electron Microscopy (cryo-TEM) images of am-hydr-IrO_x, showing the a) thicker and b) thinner film sheets used for detailed imaging of the highly disordered macro-/micro-void structure.*

Supplementary Note 13. *In situ and operando Ir L_3-edge XAS experimental setup and energy calibration at the at the Cryo-EXAFS endstation at the KMC-3 beamline, BESSY II, Germany*

S13.1. Experimental setup at Cryostat endstation at KMC-3 beamline

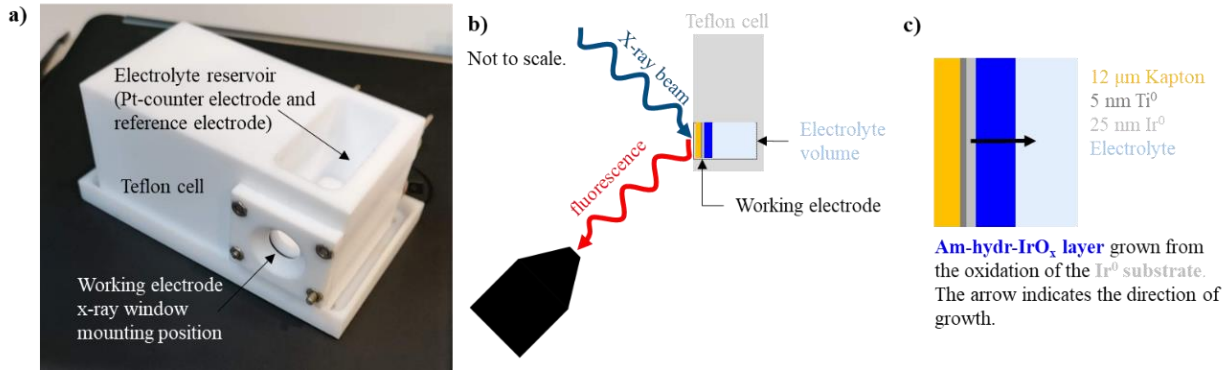

Figure S34. *in situ setup used for Ir L_3-edge XANES and EXAFS measurements at the Cryosat endstation at KMC-3, BESSY II. a) Picture of the custom-made three-electrode Feflon electrochemical cell. b) schematic of the measurement geometry, where the sample is at 45° angle with respect to the incident x-ray beam and the fluorescence detector is at 90° angle with respect to the incident x-ray beam. c) schematic of the working electrode layers. The am-hydr-IrO_x grows towards the back of the cell.*

Figure S34a depicts the custom Teflon electrochemical cell coupled to a Biologic SP-300 potentiostat and **Figure S34b** the experimental configuration of the fluorescence Ir L_3-edge XAS measurements performed at the KMC-3 beamline of BESSY II during the *in situ* growth and potential dependent transformation of am-hydr-IrO_x. The metallic Ir substrate was prepared by DC magnetron sputtering of 5 nm of Ti as an adhesion layer, followed by 25 nm of metallic Ir onto a 12 µm thick Kapton membrane (Sigma Aldrich); it also served as the X-ray transparent window (**Figure S34c**). The working electrode was attached to the side of the Teflon cell. The exposed area of the electrode to the electrolyte was 1.96 cm^2. All potentials were compensated for a 85% Ohmic drop (R ≈ 8.5 Ω).

Ir L_3-edge XAS measurements were performed in fluorescence geometry using a 13-element Ge fluorescence detector at 45° angle with respect to the sample surface (**Figure S34b**), and by integrating the intensity of the Ir Lα1 emission line. Both XANES and EXAFS data were collected during the HIROF growth at intervals during a series of cycles (0 to 1000 cycles) to track the electrochemical oxidation of the metallic Ir substrate and its transformation into am-hydr-IrO_x. After 1000 cycles of growth, a thick layer of am-hydr-IrO_x was formed and Ir L_3-edge XANES measurements were collected during potential application between 0.3 – 1.5 V_{RHE}.

S13.2. Energy calibration

Typically, for XAS experiments, energy calibration is done by the simultaneous measurement of a reference material (often a metal foil) placed downstream of the sample. Therefore, energy correction or calibration of each XAS measurement can be carried out with reference to the known absorption edge of the reference material. However, in the case of an experimental setup which does not allow for a reference material to be placed downstream of the sample (i.e., in the case of an electrochemical cell which is non-transparent to X-rays such as the one used in this work), an alternative method needs to be employed.

For this work, a 100 nm Ir^0 thin film on a Si wafer with a native SiO_2 layer was used as the reference material. This sample was regularly placed in the measurement position and measured during the course of the experiment. This gives a time-dependent external energy calibration reference.

Furthermore, given the nature of the experimental setup (that collects the signal in fluorescence mode) and the working electrode layers (see **Figure S34**), the Ir^0 thin film of the working electrode can be used as an internal energy calibration reference. The absorption edge of the XAS measurements in fluorescence geometry will be dominated by the remaining, unoxidized Ir^0 thin film due to this material being closer to the incident X-rays and the fluorescence detector (see **Figure 1d**). Furthermore, Ir^0 has a higher absorption coefficient compared to iridium oxides. The absorption coefficient (μ) depends primarily on the density of the material (ρ), the atomic number (Z), the atomic mass (A), and the x-ray energy (E)[43]:

$$\mu \approx \frac{\rho \cdot Z^4}{A \cdot E^3}$$

The absorption coefficient of Ir^0 is much larger than IrO_2 given its higher density (22.56 g/cm^3 vs. 11.66 g/cm^3 for IrO_2). Am-hydr-IrO_x also has a significantly lower density than rutile-IrO_2, hence the absorption edge of the *in situ* Ir L_3-edge XANES data will be strongly dominated by the Ir^0 species, even for low Ir^0 concentrations. For the upper limit of the growth cycles (1000 cycles), complete consumption of the Ir^0 has not occurred (x_{Ir^0} = 0.2 ± 0.1, see **Supplementary Note 11** for calculation details). Therefore given the unique sample properties, the Ir^0 thin film of the working electrode can be used as an internal energy calibration reference throughout the duration of the experiment by its adsorption edge position.

Supplementary Note 14. *In situ and operando Ir L_3-edge XAS experimental setup and excitation energy calibration at the HRPD-XAS endstation at the NOTOS beamline, ALBA, Spain*

S14.1. Experimental setup at NOTOS beamline

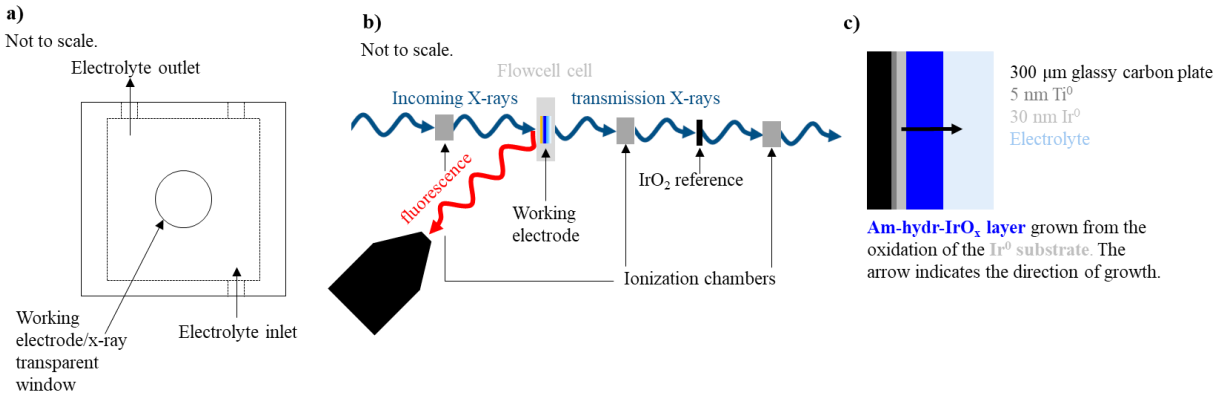

Figure S35. *in situ setup used for Ir L_3-edge XANES and EXAFS measurements at NOTOS beamline from ALBA Synchrotron. a) Schematic of the custom-made three-electrode 3D-printed electrochemical cell. b) Schematic of the measurement geometry, where the sample is at 90° angle with respect to the incident X-ray beam and the fluorescence detector is at 45° angle with respect to the incident X-ray beam. c) Schematic of the working electrode layers.*

In situ Ir L_3-edge XANES and EXAFS measurements during the *in situ* growth and potential dependent transformation of am-hydr-IrO_x was performed at the the High Resolution Powder Diffraction HRPD-XAS endstation at the NOTOS beamline from the ALBA Synchrotron Light Source facility located at Cerdanyola de Vallès (Barcelona, Spain). The synchrotron light coming from a bending magnet was first vertically collimated, then monochromated using two pairs of water-cooled Si(111) crystals, and finally focused to the sample position down to ~500 × 500 µm^2. The Ir L_3-edge XAS measurements were performed in fluorescence geometry using a 13-element energy-resolving silicon-drift fluorescence detector (Canberra) at 45° angle with respect to the incoming X-rays (**Figure S35b**). Three DC current-type ionization chambers (Oken) were used for measuring the incoming beam intensity and the IrO_2 reference in transmission mode (**Figure S35b**). The custom-made flow cell was mounted on a motorized xyz sample stage, and connected to a Biologic SP-300 potentiostat. The substrate was prepared by DC magnetron sputtering 25 nm of metallic Ir onto a 300 µm thick glassy carbon plate with a 5 nm Ti adhesion layer. This working electrode was mounted to the side of the cell. The exposed area of the electrode to the electrolyte was 0.28 cm^2. For the counter electrode, a 1 × 1 cm Pt mesh (52 mesh woven, 0.1 mm diameter wire, 99.9% Alfa Aesar) was used and a reversible hydrogen electrode (Mini HydroFlex, Gaskatel) was used as the reference electrode. Am-hydr-IrO_x was synthesized using 1000 HIROF growth cycles, while monitoring with XANES and EXAFS measurements, prior to the *in situ* Ir L_3-edge XAS measurements during potential application between 0.3 – 1.6 V_{RHE}.

S14.2. Energy calibration

A reference rutile-IrO_2 sample was placed downstream of the electrochemical cell, that due to the experiment configuration, allowed to work in transmission mode. Therefore, through the use of the three ionization chambers, during each XANES and EXAFS measurement of the sample in the electrochemical cell, a simultaneous measurement of the reference rutile-IrO_2 sample was made. This enables for any energy alignment correction due to drifts over time and alongside energy calibration with the reference material to the known adsorption edge of rutile-IrO_2.

Supplementary Note 15. *In situ Ir L_3-edge XAS obtained during the in situ growth of am-hydr-IrO_x*

S15.1. *In situ* electrochemical growth of am-hydr-IrO_x

Figure S17 depicts the CVs obtained after preparation of am-hydr-IrO_x by growth of HIROF to 1000 cycles. The slight differences between am-hydr-IrO_x prepared *ex-situ* in a beaker and in the *in situ* Teflon cell are likely due to differences in cell resistances (which were compensated). Thus the growth is not exactly the same, however reasonably close. The thickness of am-hydr-IrO_x grown in the *in situ* cell (determined following the method presented in **Supplementary Note 3**) is slightly smaller than in the beaker (300 vs 320 nm – **Figure S2**) due to slightly higher cell resistances.

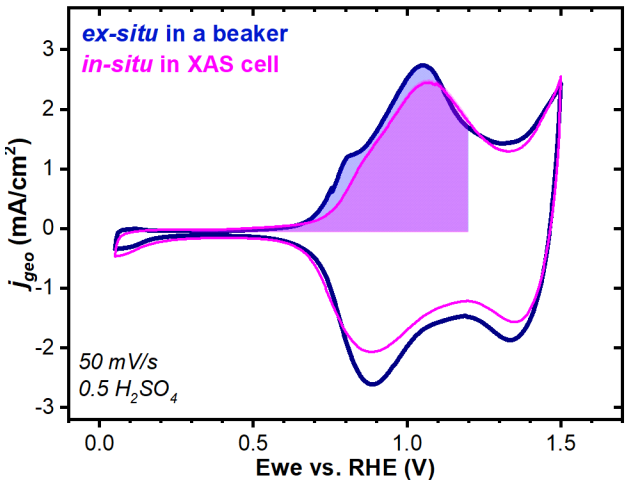

Figure S36. *in situ CV of HIROF grown to 1000 cycles (in magenta) in the Teflon electrochemical cell at the KMC-3 beamline, BESSY II, Germany compared to the CV of HIROF grown ex-situ in a beaker obtained at a scan rate of 50 mV/s in 0.5 M H_2SO_4. The colored areas under the curves represent the integration region for the charge transfer of the $Ir^{3+} \leftrightarrow Ir^{4+}$ redox couple used for the thickness estimation by Faraday's law.*

S15.2. *In situ* Ir L_3-edge XANES during *in situ* growth of am-hydr-IrO_x: analysis of the Ir L_3-edge WL position and WL intensity

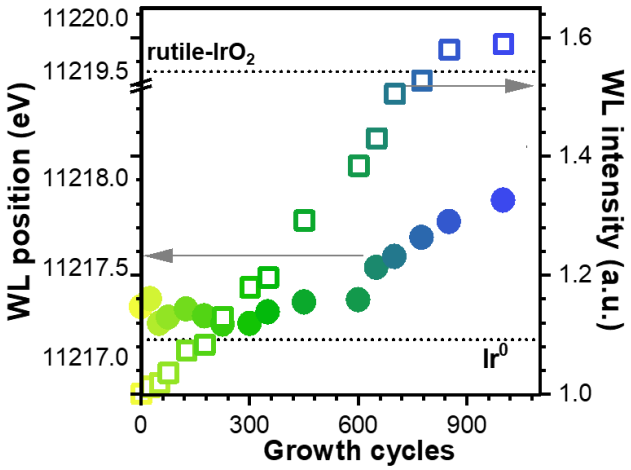

Figure S37. *Ir L_3-edge WL position shift and WL intensity increase during preparation of am-hydr-IrOx by growth up to 1000 cycles. The WL intensity is normalized to one for the XANES spectra of the starting metallic Ir substrate (i.e., 0 cycles). Horizontal dashed lines for the reference WL positions of Ir^0 and Ir^{4+} are shown for reference.*

During preparation of am-hydr-IrO_x, the WL intensity increases nearly linearly, while a pronounced WL position shift only occurs after about 600 growth cycles (**Figure S37**). In contrast, the absorption edge (E_0) remains similar to that of the metallic Ir^0 substrate throughout the growth of am-hydr-IrO_x (see main text **Figure 1e**). XAS principles specify that both the E_0 and WL position shifts toward higher excitation energies with iridium oxidation state. The WL intensity, also tied to the total Ir 5*d*-band hole count, should also monotonically increase with iridium oxidation state[44–46]. The WL position and intensity differences result from the fluorescence measurement configuration (**Figure S34**) and changing sample nature (schematic in main text **Figure 1a**). The XANES spectra contain contributions of both, the unconverted metallic Ir substrate and the grown am-hydr-IrO_x on top of it. The E_0 is influenced by the remaining metallic Ir substrate, and also serves as an internal energy calibration throughout the duration of the experiment. Similarly, the WL position is initially governed by the metallic Ir substrate (WL position Ir^0 = 11217.1 eV). As the am-hydr-IrO_x layer grows thicker, the WL position shifts to higher energy values as the am-hydr-IrO_x contribution becomes stronger, with a strong change upon reaching about 600 growth cycles, resulting in a Ir L_3-edge WL position of 11217.9 eV after 1000 growth cycles when am-hydr-IrO_x dominates the spectroscopic signal. The immediate WL intensity increase upon am-hydr-IrO_x growth signifies a change in the average Ir 5*d*-band state of the material, indicating the presence of a higher oxidation species (i.e., am-hydr-IrO_x) in the system[44–46]. Both, WL position and intensity changes thus illustrate that an oxidation process is taking place, converting Ir^0 into am-hydr-IrO_x. Due to the dual-species system, in this study the WL position is chosen as the metric to observe.

S15.3. *In situ* Ir L_3-edge EXAFS spectra obtained during *in situ* growth of am-hydr-IrO_x

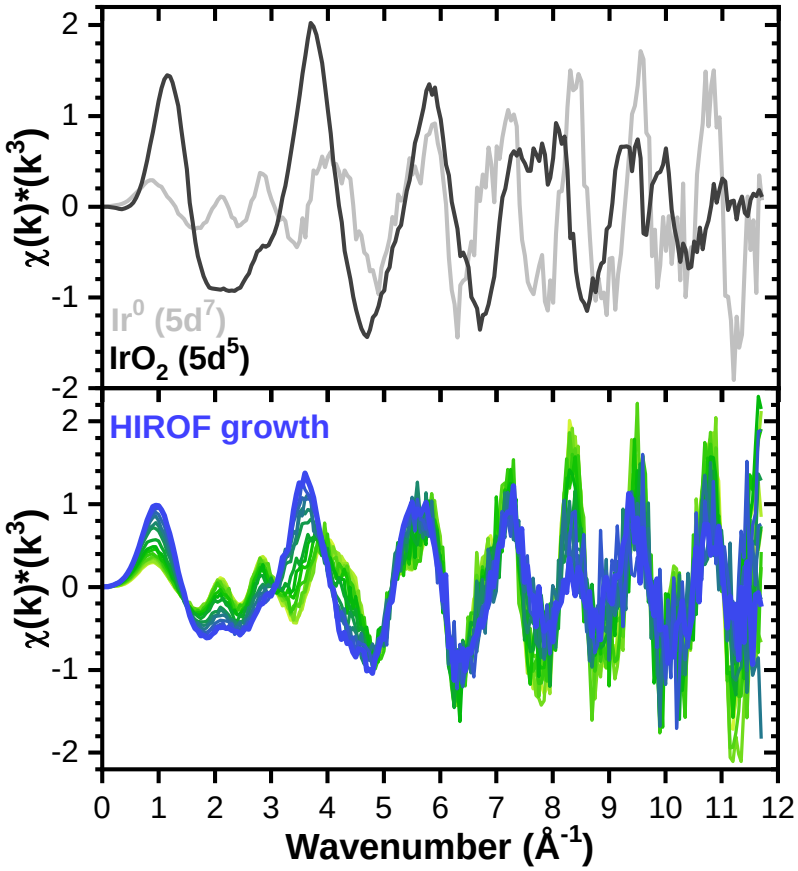

Figure S38. *k^2-weighted EXAFS spectra of the a) rutile-IrO_2 and Ir^0 references and b) of the in situ HIROF growth up to 1000 cycles from a metallic Ir substrate. These measurements were collected at the KMC-3 beamline, BESSY II, Germany.*

Supplementary Note 16. *Operando Ir L_3-edge XANES and EXAFS of am-hydr-IrO_x under potential applications*

S16.1. *Operando* Ir L_3-edge XANES spectra of am-hydr-IrO_x under potential applications

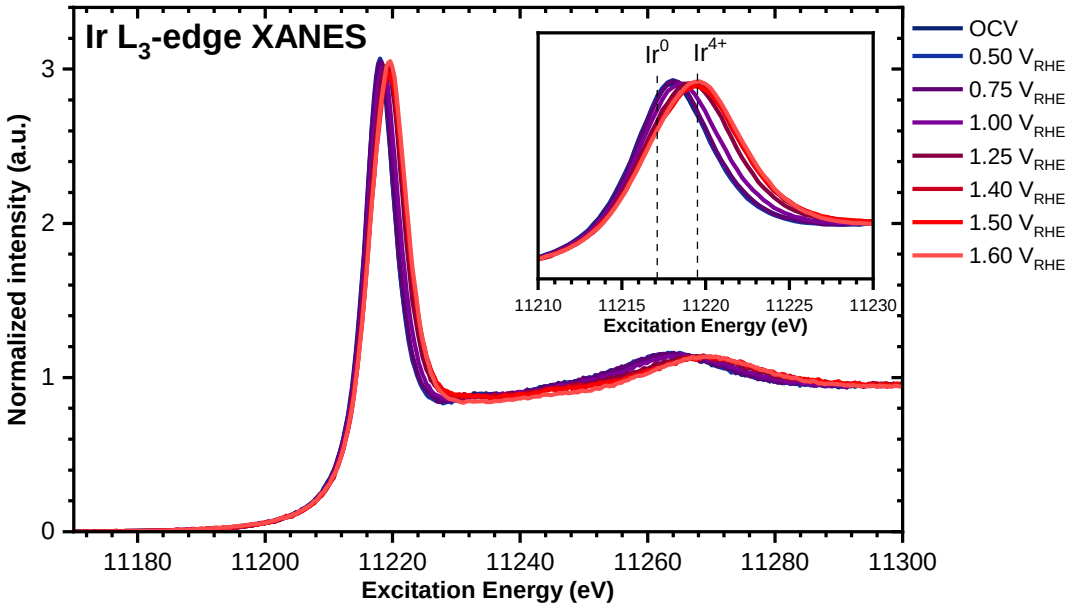

Figure S39. *Operando Ir L_3-edge XANES of HIROF at applied potential collected at the NOTOS beamline, ALBA, Spain. Vertical dashed lines indicate the WL positions of Ir^0 and Ir^{4+}.*

S16.1. *Operando* Ir L_3-edge EXAFS spectra of am-hydr-IrO_x under potential applications

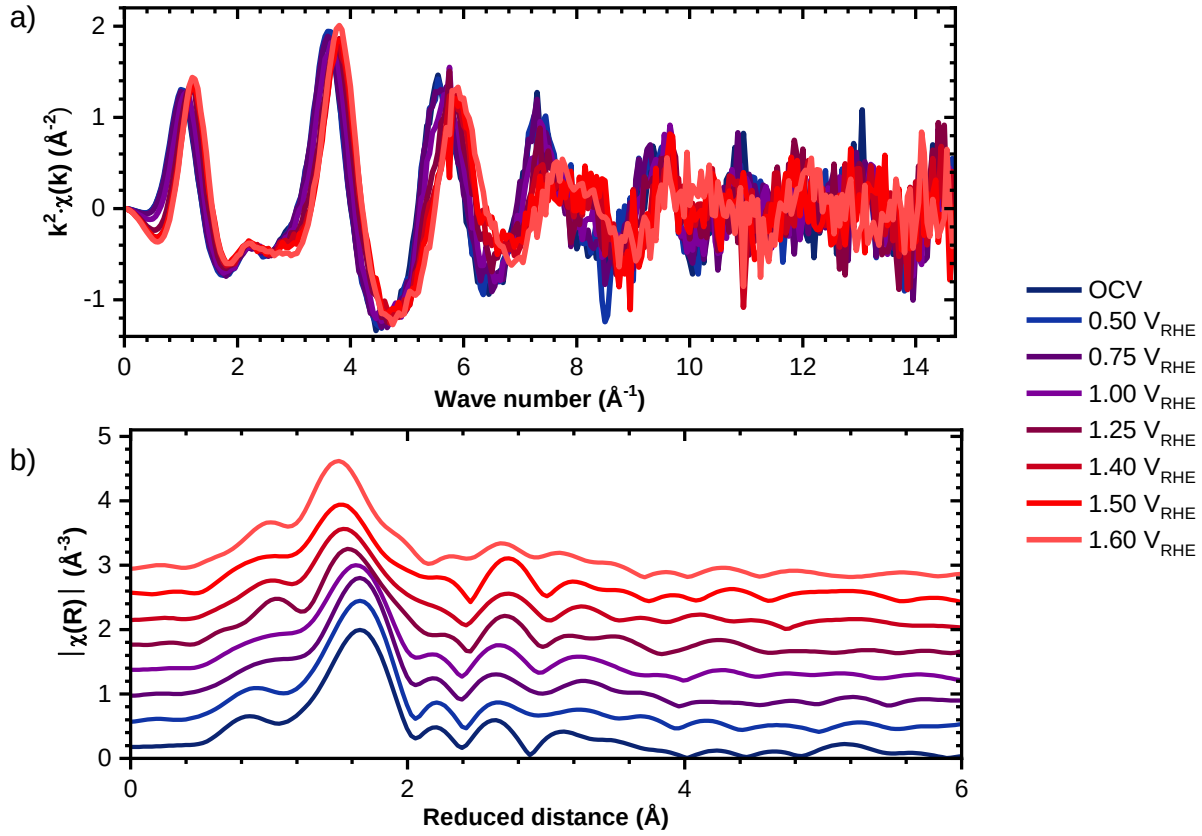

Figure S40. *a) Operando k^2-weighted Ir L_3-dge EXAFS spectra and b) their Fourier transforms (FTs) of HIROF at applied potentials collected at the NOTOS beamline, ALBA, Spain.*

Supplementary Note 17. *Comparison of the in situ Ir L_3-edge XAS collected at KMC-3 and NOTOS beamlines*

S17.1 Comparison of *in situ* Ir L_3-edge XANES data from KMC-3 and NOTOS beamlines during *in situ* growth of am-hydr-IrO_x

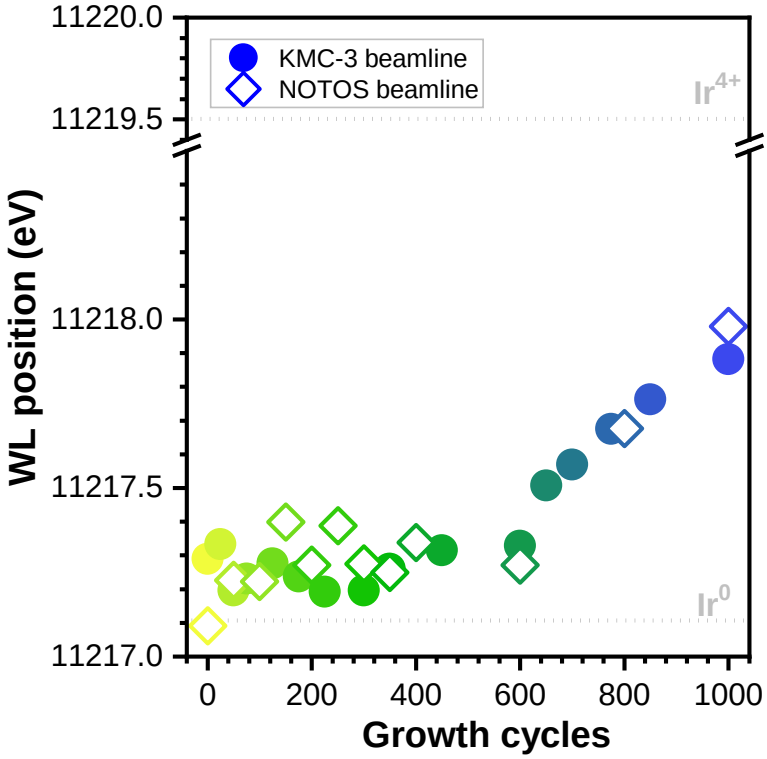

Figure S41. *Comparison of the in situ Ir L_3-edge WL positions during am-hydr-IrO_x growth up to 1000 cycles obtained at KMC-3 (circles) and NOTOS (diamonds) beamlines.*

S17.2 Comparison of *operando* Ir L_3-edge XANES data from KMC-3 and NOTOS beamlines during potential application (0.3 – 1.6 V_{RHE}) of am-hydr-IrO_x

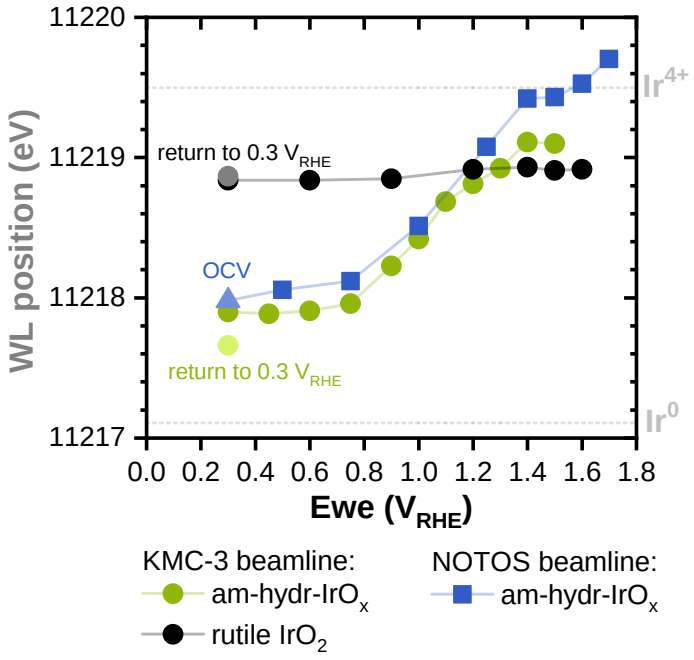

Figure S42. *Electronic structure of rutile-IrO_2 and HIROF from operando Ir L_3-edge XANES at applied potentials. The WL positions of the materials as a function of applied potential collected at the KMC-3 (circles) and NOTOS (squares) beamlines are shown. The KMC-3 beamline protocol was stepped XANES in the region 0.3 – 1.6 V_{RHE} (shown by the circles) and then returning to 0.3 V_{RHE} (shown as the lighter circles). The WL position at OCV (~ 0.3 V_{RHE}) for am-hydr-IrO_x measured at NOTOS is shown as a triangle. Horizontal grey lines indicate the WL positions of Ir^0 and Ir^{4+} standards.*

Supplementary Note 18. *EXAFS fittings of the Ir^0 and IrO_2 standards*

Using the electronic structures of face-centred-cubic (*fcc*) Ir^0 and the tetragonal IrO_2 structure EXAFS fittings of the Ir^0 and rutile-IrO_2 references were performed. The interatomic distances and CNs of these shells are listed in **Table S6**. For rutile-IrO_2, due to its tetragonal nature, the first oxygen shells are located at two distances, 1.94 Å and 2.00 Å. Likewise, the second iridium shells are located at two distances. The first shell iridium scattering path of elemental Ir is termed 'Ir^0-Ir^0' to differentiate it from the (second) shell iridium scattering pathways of IrO_2, termed 'Ir-Ir'.

***Table S6**. Shells, Coordination numbers (CNs) and interatomic distances of the rutile-IrO_2 and elemental Ir structures used for the fits of the Ir L_3-edge EXAFS data.*

	Shell	Bond	Coordination number (*CN*)	Interatomic distances (***R***) / Å
Rutile IrO_2†*	1	Ir-O	2	1.94
	2	Ir-O	4	2.00
	3	Ir-Ir	2	3.15
	4	Ir-Ir	8	3.55
fcc elemental Ir†**	1	Ir^0-Ir^0	12	2.71

†Generated in Atoms from the IFEFFIT package[27] based on data retrieved from the Materials Project for *IrO_2 (mp-2327) and **Ir (mp-101) from database version v2022 10.28

Larch software [25] was used to perform the EXAFS fits of the Ir L_3-edge EXAFS data of the Ir^0 and IrO_2 references over k = 3 – 11 $Å^{-1}$ and for R = 1 – 2.1 and R = 1 – 3.5 Å respectively; this includes only the first-shell Ir-O and Ir^0-Ir^0 scattering pathways. The EXAFS fittings are reported in **Figure S43** along with the fitting parameters in **Table S7**.

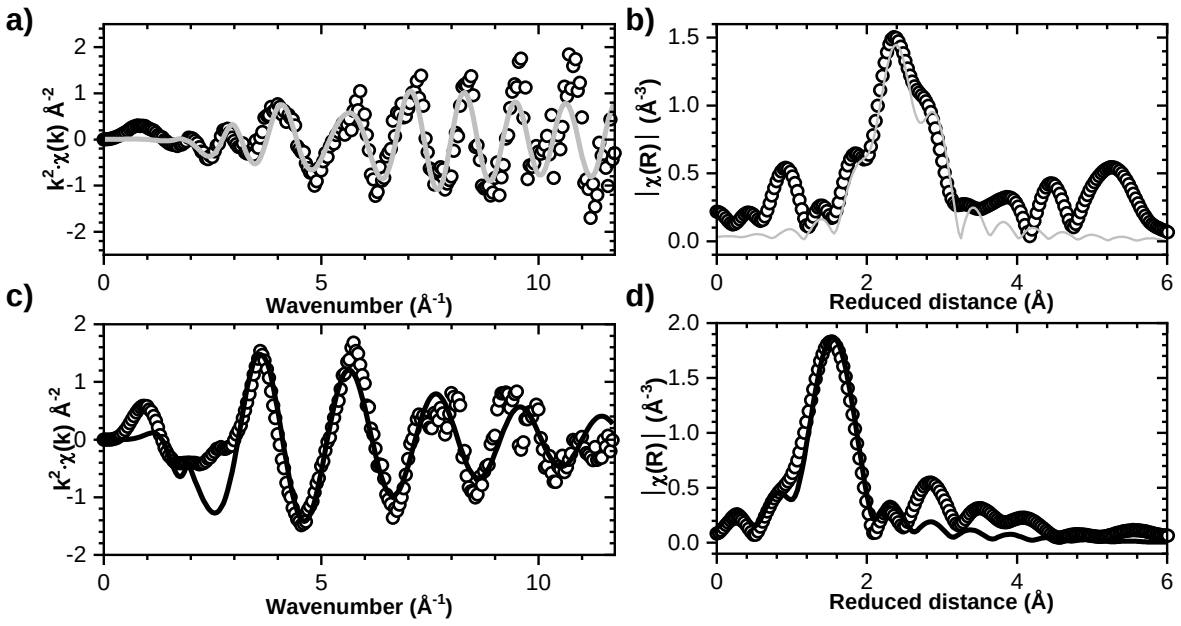

Figure S43. *k^2-weighted Ir L_3-edge EXAFS spectra and b) Fourier transformed k^2-weighted spectra of the Ir^0 (a-b) and IrO_2 (c-d) references. The experimental (open circles) and fits (solid lines) are shown.*

Table S7*. Fit parameters for the Ir L_3-edge EXAFS data of the Ir^0 and IrO_2 references in the range of k = 3 – 11 $Å^{-1}$, and R = 1 – 3.5 Å and R = 1 – 2 Å, respectively.*

Sample	Shell	N	σ^2 ($Å^2$)	ΔE_0 (eV)	R (Å)	R-factor	χ^2
Ir^0 reference	Ir-Ir	12	0.0040 ± 0.0010	9.43 ± 1.43	2.71 ± 0.01	0.03	4.2E-14
IrO_2 reference	Ir-O	2	0.0016 ± 0.0021	16.2 ± 2.1	1.96 ± 0.01	0.02	1.7E-17
	Ir-O	6	0.0016 ± 0.0021		1.99 ± 0.01		

The Debye-Waller (σ) parameters, energy shift (ΔE_0) and interatomic distances (R) were unconstrained.
The passive electron reduction factors (S_0^2) were determined to be **0.78 ± 0.12** for the metallic Ir standard and **0.83 ± 0.15** for rutile IrO_2 standard.

The passive electron reduction factors (S_0^2) of metallic Ir and rutile-IrO_2 were determined to be 0.78 and 0.83, respectively (reported in **Table S6**). In the fits of the Ir L_3-edge EXAFS of HIROF, the S_0^2 of the iridium oxide atomic model used for the am-hydr-IrO_x component was set to 0.83.

Supplementary Note 19. *EXAFS fits of the operando Ir L_3-edge EXAFS spectra of am-hydr-IrO_x at applied potentials between 0.30 and 1.60 V_{RHE}*

EXAFS fits were performed for the *operando* Ir L_3-edge EXAFS data of am-hydr-IrO_x at applied potentials (0.3 – 1.6 V_{RHE}). Here, the focus was only the change in the first coordination shell Ir-O bond length. A single-component model (using the nanosheet Θ_H = 0.50 ML atomic model) was used to fit the region R = 1 – 2.1 Å, where the *CN* and *R* was allowed to vary. The results of the EXAFS fits are summarized in **Table S8**.

***Table S8**. Fit parameters of the operando Ir L_3-edge EXAFS data of am-hydr-IrO_x at applied potentials fitted with the H-terminated nanosheet Θ_H = 0.50 ML structure for k = 3 – 11 $Å^{-1}$ over the range R = 1 – 2.1 Å.*

Sample	Shell	N	σ^2 ($Å^2$)	ΔE_0 (eV)	R (Å)	R-factor	χ^2
am-hydr-IrO_x pristine/OCV	Ir-O	6 ± 0.70	0.0022 ± 0.0013	16.6 ± 1.36	2.04 ± 0.01	0.01	141.19
0.50 V_{RHE}	Ir-O	6 ± 0.84	0.0019 ± 0.0016	16.63 ± 1.64	2.04 ± 0.01	0.02	151.95
1.00 V_{RHE}	Ir-O	6 ± 0.00	0.0022 ± 0.0015	16.89 ± 1.51	2.04 ± 0.01	0.02	97.37
1.25 V_{RHE}	Ir-O	6 ± 0.80	0.0036 ± 0.0016	16.87 ± 1.5	2.02 ± 0.01	0.01	94.19
1.40 V_{RHE}	Ir-O	6 ± 0.34	0.0053 ± 0.0027	17.17 ± 2.21	2.00 ± 0.02	0.03	151.75
1.50 V_{RHE}	Ir-O	6 ± 0.80	0.0062 ± 0.0019	15.61 ± 1.57	1.96 ± 0.01	0.01	90.32
1.60 V_{RHE}	Ir-O	6 ± 0.73	0.0066 ± 0.0017	14.18 ± 1.46	1.94 ± 0.01	0.01	39.77

The Debye-Waller (σ) parameters, energy shift (ΔE_0) interatomic distances (R), and coordination numbers (CN) were unconstrained.

The passive electron reduction factor (S_0^2) was determined from the Ir0 and IrO_2 standards and set to be 0.78 ± 0.12 for the metallic Ir and 0.83 ± 0.15 for the H-terminated nanosheet sheet (Θ_H = 0.50 ML) used in the fittings.

Supplementary Note 20. *Influence of explicit water interface with iridate nanosheets*

To comprehend the impact of explicit water molecules on the Ir-O bond length at the interface and to provide further rationale for our calculation setup using an implicit solvation model instead, we utilize *ab initio* molecular dynamics within the isothermal–isobaric (NpT) ensemble. We calculate four iridate nanosheet models, each with varying hydrogen coverages ($\Theta_H = 0.00$, 0.125, 0.25, and 0.50 ML), incorporating explicit water.

To systematically generate a water model for our simulation setup, we initially conduct classical force-field molecular dynamics using the empirical TIP3P water model [47]. Adjusting the *z* lattice of the periodic unit-cell of 64 water molecules based on the optimized *x* and *y* lattice parameters of the $\begin{pmatrix} 4 & 0 \\ -2 & 4 \end{pmatrix}$ nanosheet supercell, we aim to achieve a density of 1 g/cc within the enclosed water molecules. Following this, we equilibrate the system for 100 fs with a timestep of 0.01 fs, followed by an additional 10 ps with a timestep of 1 fs in the NVT ensemble at 300K, ensuring the generation of a stable trajectory. A critical criterion for stability is that the water dipoles should exhibit no specific orientation when the system demonstrates bulk-like behavior. To assess this, we analyze the distribution of the cosine of the water dipoles concerning the *z*-direction. The obtained distribution proved to be isotropic, as illustrated in **Figure S44**.

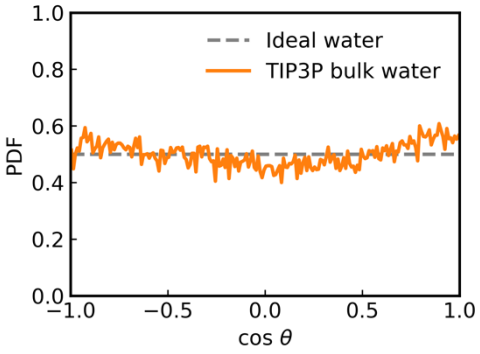

Figure S44. *The probability density function of the cosine of the dipole angle with respect to the z-axis is plotted for a 64-water model, scaled to match the supercell size of the iridate nanosheet. The dashed line represents the probability density for an ideally uncorrelated distribution.*

We further conduct a 10 ps NVT ab initio molecular dynamics simulation at 350 K, employing the PBE functional with TS-vdW correction. The resulting trajectory from the final bulk water simulation is then applied to the four iridate models. All interface models undergo a 10 ps equilibration with a timestep of 0.5 fs in the Berendsen NpT ensemble at 350 K and the desired pressure of 1 atm. The time constants for Berendsen temperature and pressure coupling are set to 0.1 and 1 ps, respectively. The last 5 ps of the trajectories are used for production.

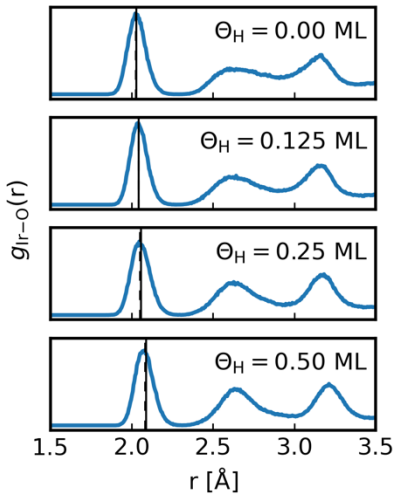

Figure S45. *The simulated Ir-O radial distribution function $g_{Ir-O}(r)$ of water-iridate interface models is presented with various hydrogen coverages. The last 5 ps trajectories are utilized for the production. Vertical dashed lines denote the average first coordination shell Ir-O bond length in explicit water-iridate interface models, while solid lines represent the same Ir-O bond length from DFT-optimized iridate nanosheets with implicit solvent.*

Figure S45 displays the simulated Ir-O radial distribution function (RDF) of water-iridate interface models with varying hydrogen coverages. The average first coordination shell Ir-O bond length from these interface models aligns well with the Ir-O bond length obtained from the DFT-optimized iridate nanosheets with implicit solvent.

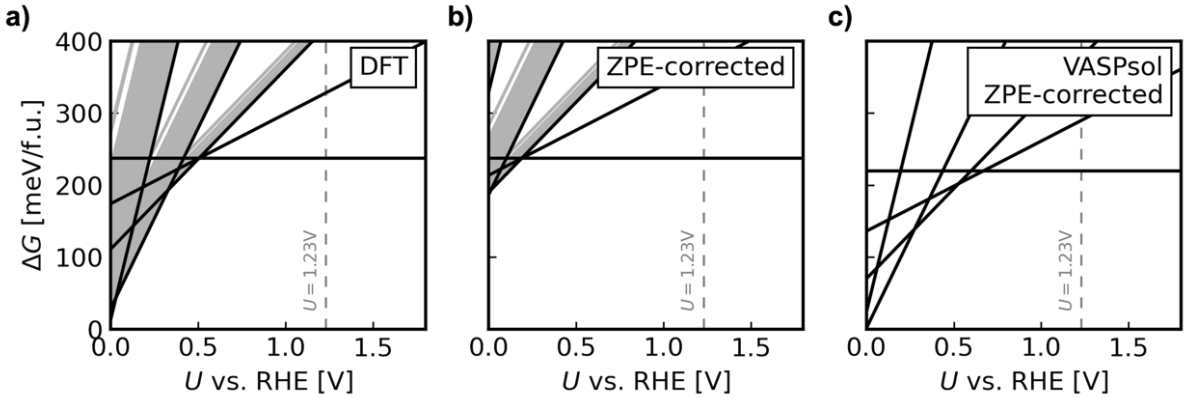

Figure S46. *Phase diagrams illustrating the stability of sheet surface terminations with varying H coverage as a function of the applied potential U (vs RHE). The diagrams depict a) pure DFT results, b) Zero Point Energy (ZPE)-corrected results for adsorbed hydrogen, and c) those incorporating implicit solvent effects.*

References

1. McIntyre, J. D. E., Peck, W. F. & Nakahara, S. Oxidation State Changes and Structure of Electrochromic Iridium Oxide Films. *Journal of The Electrochemical Society* **127**, 1264–1268 (1980).
2. Schneider, C. A., Rasband, W. S. & Eliceiri, K. W. NIH Image to ImageJ: 25 years of image analysis. *Nature Methods* **9**, 671–675 (2012).
3. Gottesfeld, S. & Srinivasan, S. Electrochemical and optical studies of thick oxide layers on iridium and their electrocatalytic activities for the oxygen evolution reaction. *Journal of electroanalytical Chemistry and Interfacial Electrochemistry* **86**, 89–104 (1978).
4. Burke, L. D. & O'Sullivan, E. J. Oxygen gas evolution on hydrous oxides — An example of three-dimensional electrocatalysis? *Journal of Electroanalytical Chemistry1* **117**, 155–160 (1981).
5. Kasian, O. *et al.* Degradation of iridium oxides via oxygen evolution from the lattice: Correlating atomic scale structure with reaction mechanisms. *Energy and Environmental Science* **12**, 3548–3555 (2019).
6. Geiger, S. *et al.* Activity and Stability of Electrochemically and Thermally Treated Iridium for the Oxygen Evolution Reaction. *Journal of The Electrochemical Society* **163**, F3132–F3138 (2016).
7. Geiger, S. *et al.* The stability number as a metric for electrocatalyst stability benchmarking. *Nature Catalysis* **1**, 508–515 (2018).
8. Cherevko, S., Geiger, S., Kasian, O., Mingers, A. & Mayrhofer, K. J. J. Oxygen evolution activity and stability of iridium in acidic media. Part 1. - Metallic iridium. *Journal of Electroanalytical Chemistry* **773**, 69–78 (2016).
9. Cherevko, S., Geiger, S., Kasian, O., Mingers, A. & Mayrhofer, K. J. J. Oxygen evolution activity and stability of iridium in acidic media. Part 2. - Electrochemically grown hydrous iridium oxide. *Journal of Electroanalytical Chemistry* **774**, 102–110 (2016).
10. El Sawy, E. N. & Birss, V. I. Nano-porous iridium and iridium oxide thin films formed by high efficiency electrodeposition. *Journal of Materials Chemistry* **19**, 8244–8252 (2009).
11. El Sawy, E. N. & Birss, V. I. A Comparative Study of the Electrodeposition of Nanoporous Ir and Pt Thin Films. *Journal of The Electrochemical Society* **160**, D386–D393 (2013).
12. Favaro, M. *et al.* Spectroscopic analysis with tender X-rays: SpAnTeX, a new AP-HAXPES end-station at BESSY II. *Surface Science* **713**, 121903 (2021).
13. Kötz, R. Anodic Iridium Oxide Films. *Journal of The Electrochemical Society* **131**, 72 (1984).
14. Pickup, P. G. & Birss, V. I. A model for anodic hydrous oxide growth at iridium. *Journal of Electroanalytical Chemistry* **220**, 83–100 (1987).
15. Pfeifer, V. *et al.* The electronic structure of iridium and its oxides. *Surface and Interface Analysis* **48**, 261–273 (2016).
16. Pfeifer, V. *et al.* The electronic structure of iridium oxide electrodes active in water splitting. *Physical Chemistry Chemical Physics* **18**, 2292–2296 (2016).
17. Pfeifer, V. *et al.* Reactive oxygen species in iridium-based OER catalysts. *Chemical Science* **7**, 6791–6795 (2016).
18. Moulder, J. F., Stickle, W. F., Sobol, P. E. & Bomben, K. D. *Handbook of X-Ray Photoelectron Spectroscopy*. (Eden Prairie, MN, 1992).
19. Freakley, S. J., Ruiz-Esquius, J. & Morgan, D. J. The X-ray photoelectron spectra of Ir, IrO_2 and $IrCl_3$ revisited. *Surface and Interface Analysis* **49**, 794–799 (2017).
20. Kötz, E. R. & Neff, H. Anodic iridium oxide films: An UPS study of emersed electrodes. *Surface Science* **160**, 517–530 (1985).
21. Newville, M. *et al.* LMFIT: Non-Linear Least-Square Minimization and Curve-Fitting for Python (0.8.0). *Zenodo* Preprint at https://dx.doi.org/10.5281/zenodo.11813 (2016).
22. Major, G. H., Shah, D., Fernandez, V., Fairley, N. & Linford, M. R. Advanced Line Shapes in X-Ray Photoelectron Spectroscopy II. The Finite Lorentzian (LF) Line Shape. *Vacuum Technology & Coating* 35–40 (2020).
23. Trzhaskovskaya, M. B., Nefedov, V. I. & Yarzhemsky, V. G. Photoelectron angular distribution parameters for elements Z = 55 to Z = 100 in the photoelectron energy range 100-5000 eV. *Atomic Data and Nuclear Data Tables* **82**, 257–311 (2002).
24. Mom, R. V. *et al.* Operando Structure-Activity-Stability Relationship of Iridium Oxides during the Oxygen Evolution Reaction. *ACS Catalysis* **12**, 5174–5184 (2022).
25. Newville, M. Larch: An Analysis Package for XAFS and Related Spectroscopies. *Journal of Physics: Conference Series* **430**, 012007 (2013).
26. Gottesfeld, S. & Srinivasan, S. Electrochemical and optical studies of thick oxide layers on iridium and their electrocatalytic activities for the oxygen evolution reaction. *Journal of electroanalytical Chemistry and Interfacial Electrochemistry* **86**, 89–104 (1978).
27. Böld, W. & Breiter, M. Untersuchung des anodischen aufbaus und der kathodischen reduktion der sauerstoffbelegung an glatten pt-elektroden. *Electrochimica Acta* **5**, 145–160 (1961).
28. Capon, A. & Parsons, R. The effect of strong acid on the reactions of hydrogen and oxygen on the noble metals. A study using cyclic voltammetry and a new teflon electrode holder. *Journal of Electroanalytical Chemistry and Interfacial Electrochemistry* **39**, 275–286 (1972).

29. Otten, J. M. & Visscher, W. The anodic behaviour of iridium: I. The effect of potential cycling. *Journal of Electroanalytical Chemistry and Interfacial Electrochemistry* **55**, 1–11 (1974).
30. Otten, J. M. & Visscher, W. The anodic behaviour of iridium: II. The oxygen coverage. *Journal of Electroanalytical Chemistry and Interfacial Electrochemistry* **55**, 13–21 (1974).
31. Conway, B. E. & Mozota, J. Surface and bulk processes at oxidized iridium electrodes-II. Conductivity-switched behaviour of thick oxide films. *Electrochimica Acta* **28**, 9–16 (1983).
32. - Geiger, S. - Stability investigations of iridium-based catalysts towards acidic water splitting. (2017).
33. Birss, V. I., Bock, C. & Elzanowska, H. Hydrous Ir oxide films: the mechanism of the anodic prepeak reaction. *Canadian Journal of Chemistry* **75**, 1687–1693 (1997).
34. Ankudinov, A. L., Ravel, B., Rehr, J. J. & Conradson, S. D. Real-space multiple-scattering calculation and interpretation of x-ray-absorption near-edge structure. *Physical Review B* **58**, 7565–7576 (1998).
35. Hjorth Larsen, A. *et al.* The atomic simulation environment—a Python library for working with atoms. *Journal of Physics: Condensed Matter* **29**, 273002 (2017).
36. Rossmeisl, J., Qu, Z. W., Zhu, H., Kroes, G. J. & Nørskov, J. K. Electrolysis of water on oxide surfaces. *Journal of Electroanalytical Chemistry* **607**, 83–89 (2007).
37. Nørskov, J. K. *et al.* Origin of the Overpotential for Oxygen Reduction at a Fuel-Cell Cathode. *The Journal of Physical Chemistry B* **108**, 17886–17892 (2004).
38. Reuter, K. & Scheffler, M. Composition, structure, and stability of RuO_2(110) as a function of oxygen pressu. *Physical Review B* **65**, 035406 (2001).
39. Plaisance, C. P., Reuter, K. & van Santen, R. A. Quantum chemistry of the oxygen evolution reaction on cobalt(ii,iii) oxide – implications for designing the optimal catalyst. *Faraday Discussions* **188**, 199–226 (2016).
40. Plaisance, C. P., Beinlich, S. D. & Reuter, K. Kinetics-Based Computational Catalyst Design Strategy for the Oxygen Evolution Reaction on Transition-Metal Oxide Surfaces. *The Journal of Physical Chemistry C* **123**, 8287–8303 (2019).
41. Dickens, C. F., Kirk, C. & Nørskov, J. K. Insights into the Electrochemical Oxygen Evolution Reaction with ab Initio Calculations and Microkinetic Modeling: Beyond the Limiting Potential Volcano. *The Journal of Physical Chemistry C* **123**, 18960–18977 (2019).
42. Reier, T. *et al.* Molecular insight in structure and activity of highly efficient, low-Ir Ir-Ni oxide catalysts for electrochemical water splitting (OER). *Journal of the American Chemical Society* **137**, 13031–13040 (2015).
43. Newville, M. 2. Fundamentals of XAFS. *Spectroscopic Methods in Mineralogy and Material Sciences* 33–74 (2014) doi:10.1515/9781614517863.33.
44. Velasco-Vélez, J. J. *et al.* Electrochemically active Ir NPs on graphene for OER in acidic aqueous electrolyte investigated by in situ and ex situ spectroscopies. *Surface Science* **681**, 1–8 (2019).
45. Nong, H. N. *et al.* A unique oxygen ligand environment facilitates water oxidation in hole-doped IrNiOx core–shell electrocatalysts. *Nature Catalysis* **1**, 841–851 (2018).
46. Velasco-Vélez, J. *et al.* Surface constrained electron-hole rich species active in the electrocatalytic water splitting. (2020) doi:https://doi.org/10.21203/rs.3.rs-118932/v1.
47. Jorgensen, W. L., Chandrasekhar, J., Madura, J. D., Impey, R. W. & Klein, M. L. Comparison of simple potential functions for simulating liquid water. *The Journal of Chemical Physics* **79**, 926–935 (1983).